

Global ENSO Modulation of MJO and its Impacts on South America

Laís G. Fernandes

Federal University of Parana: Universidade Federal do Parana

Alice Marlene Grimm (✉ grimm@fisica.ufpr.br)

Universidade Federal do Parana <https://orcid.org/0000-0002-9056-4656>

Research Article

Keywords: ENSO-MJO Interaction, South American monsoon, Precipitation, Extreme events, Teleconnections.

Posted Date: February 25th, 2022

DOI: <https://doi.org/10.21203/rs.3.rs-908939/v1>

License:   This work is licensed under a Creative Commons Attribution 4.0 International License.

[Read Full License](#)

Abstract

Changes in the Madden-Julian Oscillation (MJO) and its impacts on the South American monsoon season during different El Niño-Southern Oscillation (ENSO) states (El Niño – EN, La Niña – LN, neutral – NT) are analyzed in the global context of the MJO propagating anomalies of convection and circulation. The background ENSO-related anomalies influence several aspects of MJO (relative occurrence of phases, propagation, convection and teleconnections), and therefore modify the MJO impacts on South America (SA), such as precipitation anomalies and frequency of extreme events, as well as their temporal distribution throughout the MJO cycle. Changes include: (1) a delay in the peak of the teleconnections between central-eastern Pacific and SA, from MJO_{phase8} in LN to MJO_{phase1} in EN; (2) enhanced MJO convection in the central-east subtropical South Pacific in MJO_{LN}phases7+8 and a little further east in MJO_{EN}phases8+1, in a region efficient in generating tropics-extratropics teleconnections to SA, producing rainfall anomalies over Central-East SA (CESA), especially the South Atlantic Convergence Zone (SACZ), strongest one phase earlier in LN (MJO_{LN}phase8) than in EN (MJO_{EN}phase1), and a little shifted east in the latter than in the former; (3) predominant increase (or reduction) in the frequency of extreme events over densely populated SA regions where both ENSO and MJO contribute in the same direction, with the greatest increase over CESA (including SACZ) during EN, in MJO_{EN}phase1, and over Southeast SA (SESA), in MJO_{EN}phase3; (4) enhanced amplitude in both states, EN and LN, of the first continental intraseasonal dipole-like mode of precipitation variability between CESA and SESA, with maximum opposite anomalies in CESA, the center with largest amplitude, in phases 1 and 4 for EN, and phases 8 and 5 for LN. Significant effects can also be observed in other regions, as northeast and northwest SA.

1 Introduction

El Niño-Southern Oscillation (ENSO) and Madden-Julian Oscillation (MJO), respectively the main global interannual and intraseasonal climate variability modes, have been recognized as affecting significantly the rainfall over South America (SA). This influence is exerted through tropics-tropics and tropics-extratropics teleconnections, especially by producing anomalous Walker circulation and Rossby waves (equatorial and extratropical) that affect SA (Grimm and Ambrizzi 2009; Grimm 2019; Cai, McPhaden, Grimm et al. 2020).

The influence of ENSO on the South American climate has been analyzed by many studies, some on a continental scale, others over Brazil or specific regions in SA (e.g., Ropelewski and Halpert 1987; Aceituno 1988; Rao and Hada 1990; Grimm, Ferraz and Gomes. 1998; Grimm, Barros and Doyle. 2000; Grimm 2003, 2004, 2011). On an annual average, it produces an anomalous precipitation dipole between northeast and southeast SA, with the former (latter) region displaying negative (positive) rainfall anomalies during El Niño episodes. However, the impacts show great seasonal and spatial variation throughout the ENSO cycle (e.g., Grimm 2011). They may also depend on the position of the largest sea surface temperature (SST) anomalies in the equatorial Pacific (Central or East ENSO), although the largest differences between these two different ENSO types happen in austral autumn of the year

following the beginning of an event (Tedeschi, Grimm and Cavalcanti 2015; 2016; Cai et al. 2020). ENSO is the main source of interannual climate variability in SA and has been associated with extreme rainfall events, floods and droughts in several regions of the continent (Grimm and Tedeschi 2009; Grimm 2018).

The impacts of the MJO in the austral summer on the South American monsoon season, have been recently analyzed in the global context of the MJO propagating anomalies of convection and circulation, regarding precipitation anomalies, extreme events and the teleconnections that produce and are produced by the South American MJO-related anomalies, besides its possible role in the MJO cycle (Grimm 2019). There are very significant impacts in certain MJO phases, producing average precipitation anomalies that exceed one third of the climatological precipitation in the SA monsoon core region and doubling the frequency of extreme precipitation events in very populated regions. The influence of tropical and extratropical teleconnections and effect of topography were described. Previous studies have shown aspects of the MJO impacts on the South Atlantic Convergence Zone (SACZ, e.g., Paegle, Byerle and Mo 2000; Carvalho, Jones and Liebmann 2004; Hirata and Grimm 2015), on equatorial Brazil (Souza and Ambrizzi 2006), or on the probability of weekly-averaged rainfall exceeding the upper tercile (Alvarez et al. 2015).

Although there are studies showing that the MJO activity can influence ENSO by initiating El Niño events (e.g., Zhang and Gottschalck 2002; Hendon et al. 2007; Pohl and Matthews 2007), here the focus is on the modulation of the intraseasonal MJO and its impacts by the interannual ENSO. Some studies have analyzed the ENSO-driven variations in the characteristics of MJO itself. While some of them suggest that the amplitude of the MJO activity is not significantly affected by ENSO (Slingo et al. 1999; Hendon, Zhang and Glick 1999; Kessler 2001), there are results indicating that El Niño events shift the MJO activity eastward into the central Pacific, expanding the longitudinal domain of its convective activity and changing propagation speed (Fink and Speth 1997; Hendon, Zhang and Glick. 1999; Kessler 2001; Tam and Lau 2005; Wei and Ren 2019). Other studies have analyzed the ENSO-driven modulation of the MJO impacts on several regions and of its teleconnections (Roundy et al. 2010; Moon et al. 2011; Ghelani et al. 2017; Lee et al. 2019; Arcodia, Kirtman and Siqueira. 2020; Tseng, Maloney and Barnes 2020). It is convenient to remind that the modulation of the MJO impacts by ENSO can change the characteristics of the MJO itself, especially in regions with stronger MJO-related anomalies, since the modulation of its convection anomalies and teleconnections may modify some MJO characteristics such as its propagation and structure.

The present analysis includes an assessment of the global changes produced by ENSO in the MJO cycle in terms of anomalous convection and circulation, since these are useful to understand the reasons of the changes produced by ENSO in the MJO impacts on SA. Then the investigation addresses the ENSO-driven modulation of the MJO impacts on SA during the peak monsoon season (December-January-February, DJF), which is the rainy season over most of SA and also the season of strongest MJO and its impacts on SA. These impacts are characterized with regard to circulation and convection (OLR) anomalies, precipitation anomalies, frequency of extreme events, and the main MJO-related teleconnections affecting SA. Furthermore, changes in the amplitude of the rainfall response to MJO in

the action centers of the dipolar mode representing the largest intraseasonal variance over SA are also assessed.

ENSO can affect the MJO impacts through the modification of the MJO convective anomalies and the atmospheric basic state through which the perturbations propagate, affecting the physical mechanisms by which MJO influences rainfall variability in SA. The analysis goes beyond the composites of total anomalies in some MJO phases for the three ENSO states, Neutral, El Niño and La Niña (NT, EN, LN), since it isolates the MJO impacts in each of these states.

Although some studies use extended 6 months warm or cold season for analysis, we chose to focus on the peak monsoon season in SA (DJF), not including parts of spring and autumn, since the ENSO impacts on SA in spring, summer and autumn vary significantly. For instance, the precipitation anomalies associated with EN and LN tend to reverse their sign between spring and following summer due to land-atmosphere interactions in Central-East Brazil, a region very affected by MJO in SA (Grimm 2003, 2004; Grimm et al. 2007; Grimm and Zilli 2009). Furthermore, also MJO has different rainfall responses over SA in spring, summer and autumn (e.g., Alvarez et al. 2015). As this may produce significant differences in the ENSO modulation of the MJO-rainfall relationship, it is convenient to focus on a season with more homogeneous behavior regarding rainfall variability related to MJO and ENSO. Another distinctive aspect of the present study is the use of observed daily rainfall gauge data. Gridded precipitation data over SA may underestimate extreme precipitation events (Hirata and Grimm, 2018).

The proposed assessment of the modulation of the MJO impacts on South American by ENSO phases is important for subseasonal prediction (Grimm, Hakoyama and Scheibe 2021) and necessary for validating the models' capability in representing the MJO impacts and its teleconnections in distinct backgrounds associated with ENSO. The low-frequency variability associated with ENSO can modify the seasonal background flow, affecting the distribution, strength and propagation of the intraseasonal oscillation and the extratropical teleconnection patterns. MJO and ENSO do not act independently and composite anomalies associated with their simultaneous action are not explained by simple linear combinations of composites based on the MJO and ENSO separately (as also shown by Roundy et al. 2010; Ghelani et al. 2017). ENSO acts to modulate interannually the intraseasonal response of rainfall due to the MJO and the associated teleconnections. To emphasize the modulation by the ENSO influence on the basic state, we analyze the MJO cycle and its impacts on SA for different ENSO states: NT, EN, and LN, and remove the ENSO-related anomalies from the analyzed composite anomalies.

Section 2 describes the data and methodology used. Section 3 defines the ENSO states and the changes they introduce in the basic state, besides a statistics of the MJO phases in each ENSO state. Section 4 shows the MJO impacts in ENSO NT state, while Section 5 shows them in EN and LN states. Section 6 assesses the ENSO-driven changes in the amplitude of the rainfall response to MJO in the action centers of the dipolar mode representing the largest intraseasonal variance of the summer monsoon precipitation over SA. The summary and conclusions are presented in Section 7.

2 Data And Methodology

2.1 Data

A vast set of rain gauge daily precipitation data between 1979 and 2009, from the Brazilian Water Agency (ANA) and other hydrometeorological institutes in SA, is used in the analysis (Grimm 2019). The data are verified to find aleatory and systematic errors, and tested regarding seasonal climatology, ENSO phases and comparison with neighbor stations (Grimm and Saboia 2015). The Liebmann and Allured (2005) gridded precipitation data is also used to cover the extreme northern SA. Both precipitation datasets are gridded to 1°.

The other atmospheric variables analyzed are the outgoing longwave radiation (OLR) (Liebmann and Smith 1996) and wind data at 850 hPa and 200 hPa from NCEP/NCAR reanalysis (Kalnay et al. 1996), which was chosen for displaying circulation anomalies very consistent with the observed precipitation anomalies in Grimm (2019). Data from ERA-Interim reanalysis (Dee et al. 2011) give very similar results. The wind data are used to compute the zonally asymmetric streamfunction and the velocity potential (Dawson 2016). The streamfunction represents better the rotational wind component in the tropics than the geopotential height, and the velocity potential shows tropical convergence/divergence centers, which are key features of the tropical MJO circulation. The analysis starts at 1979 to avoid biases in the zonally-averaged OLR in the deep tropics (10°N-20°S). Besides, the MJO patterns are better represented in NCEP/NCAR reanalysis after mid-1970s, when satellite observations began to be added (Slingo et al. 1999).

Global sea surface temperature (SST), used to characterize ENSO events, are from HadISST1 data set (Rayner et al. 2003) between 1950 and 2009.

2.2 Methodology

2.2.1 ENSO states

The ENSO states are classified according to the first Principal Component Analysis (PCA) rotated mode of the global SST anomalies in DJF, between 1950 and 2009, gridded to 5°. The PCA is based on a correlation matrix, and the Varimax rotation is used to obtain orthogonal rotated variability modes. The rotation facilitates the separation of modes associated with different physical processes (Richman 1986; Wilks 2006). The factor scores and the factor loadings for the first mode describe, respectively, the temporal evolution and spatial distribution of the ENSO variability mode. Factor scores above (below) 0.75 (-0.75) define positive (negative) ENSO phases, or EN (LN) states. Neutral ENSO state (NT) is defined by factor scores in between.

Using the first global SST variability mode for representing the occurrence of ENSO opposite phases is probably a more complete way of describing the ENSO effect on MJO, since this mode also includes other SST anomalies besides the Niño 3 or Niño 3.4 SST, which are frequently used as indexes to

characterize the occurrence of ENSO extreme phases. For instance, the ENSO-related anomalies in the Indian and western Pacific may be relevant for changes in convective activity there, as they occur on top of the already warm temperatures in the warm pool (Hendon, Zhang and Glick 1999). Using this mode as an index represents more completely the global anomalies associated with ENSO.

2.2.2 MJO phases

The MJO phases are defined according to the Wheeler and Hendon (2004) realtime multivariate MJO (RMM) index, computed by multivariate empirical orthogonal function (EOF) analysis of OLR and zonal wind at 850 hPa and 200 hPa averaged between 15°S and 15°N, after subtracting the annual cycle and removing the variability associated with ENSO and lower frequency. The RMM1 and RMM2 indices are evaluated by projection of the OLR and zonal winds at 850 hPa and 200 hPa onto the first combined EOFs.

The amplitude of the MJO $\left(A = \left[(RMM1)^2 + (RMM2)^2 \right]^{\frac{1}{2}} \right)$ defines the occurrence of the oscillation: when $A \geq 1$ the MJO is active and when $A < 1$ the MJO is in a neutral phase (inactive). The eight MJO phases are determined by the 45° intervals from 0° to 360° of a phase angle $\theta = \tan^{-1} \left(\frac{RMM2}{RMM1} \right)$. The

active MJO days in each MJO phase for DJF are determined for the different ENSO states (EN, LN, NT). Since the number of EN, LN and NT years is not the same, the number of active MJO days in each MJO phase is expressed as a percentage of the total number of days in each ENSO category (Section 3).

2.2.3 Anomaly composites for MJO phases in different ENSO states

The methods for calculating composite anomalies for different MJO phases are the same described in Grimm (2019), with the only difference that each ENSO state (EN, LN, NT) adds a new category of composites. The daily climatological means are calculated smoothing the daily means with a 31-day moving average, which acts as a filter to remove the spurious variance due to the 31-year sample. The daily anomalies are obtained from the difference between the observed data in each day and the daily climatological mean for the same day. These anomalies are submitted to a bandpass Lanczos filter (Duchon 1979) with 211 weights, retaining only the intraseasonal variability in the 20–90 day band. After this filtering, only the anomalies in DJF are used in the composites. The filtered anomalies do not include the direct effect from other climate variability modes (interannual, interdecadal), since we are interested in the ENSO effect on the MJO, and not in the sum of the MJO and ENSO-related anomalies over SA. Therefore, the ENSO-related anomalies are removed from the composite anomalies.

The statistical significance of the composite anomalies is assessed with the Student's t-test used to identify different means from two samples (Wilks 2006). The null hypothesis is rejected if the sample means are different, for instance, the sample mean for MJO phase 1 in EN, and the sample mean from all DJF days in 1979–2009. As the samples may exhibit serial dependence, characterized by the

autocorrelation coefficient at lag 1, termed ρ_1 , it is necessary to estimate the effective sample size

$$n = N \left(\frac{1 - \rho_1}{1 + \rho_1} \right), \text{ in which } N \text{ is the original sample size (Wilks 2006).}$$

2.2.4 Frequency of extreme precipitation events

The frequency of extreme precipitation events is also analyzed, since they are related to potential natural disasters over SA, as floods and mudslides in populous regions. The methods are similar to Grimm and Tedeschi (2009), which involve the computation of:

- the 3-day running means of precipitation, which are attributed to the central days, so that persistence is also taken into account;
- the 90th percentile of the gamma distribution adjusted to the daily precipitation data, one value for each day of the year;
- the precipitation percentile in each day of the year, for each grid point.

When this percentile exceeds the 90th percentile, it characterizes an extreme event. The proportion of extreme events (or probability of extreme event occurrence) is computed for each MJO phase and ENSO state, besides the average number of extreme events for all DJF days between 1979 and 2009. The Student's t-test is applied to assess the significance of the difference between these sample means, using the effective sample size mentioned before, since the number of extreme events is evaluated based on a 3-day running mean, and the daily data present autocorrelation. Instead of representing this difference, the ratio between these two probabilities of extreme events occurrence is displayed. It informs by which factor the climatological probability changes in each MJO phase, within each ENSO state. When it is larger (smaller) than 1, it means that the frequency of extreme events increases (decreases) by that factor in a specific MJO-ENSO scenario.

3 Enso: Changes Of Mean State And Frequency Of Mjo Phases

3.1 ENSO states

Figure 1 shows the factor loadings and the factor scores of the first rotated variability mode of global SST anomalies, obtained from PCA. Its temporal evolution and spatial distribution represent the ENSO behavior. The factor loadings show a pattern similar to the canonical ENSO events, with strong SST anomalies over central-eastern equatorial Pacific and opposite anomalies over western Pacific and the Pacific subtropics. Using the factor score threshold 0.75 (-0.75) to classify the positive (negative) ENSO phases resulted in 8 EN, 10 LN and 14 NT years (Table 1) within the 31 years analyzed.

The EN (LN) list thus obtained is similar to the strongest events, obtained with the Oceanic Nino Index (ONI), equal or greater than 0.8°C (equal or smaller than -0.8°C). This index is based on the 3-month running mean of SST anomalies in the Niño 3.4 region (5°N - 5°S , 120° - 170°W). ENSO events using ONI

threshold of $\pm 0.5^{\circ}\text{C}$ are listed in

https://origin.cpc.ncep.noaa.gov/products/analysis_monitoring/ensostuff/ONI_v5.php. Therefore, the ENSO classification obtained here is validated by two different methods, with the advantage that the PCA technique extracts the first variability mode taking into account the global SST anomalies, instead of restricting the classification to the Niño 3.4 region. The only event in Table 1 not qualified by the ONI index is the 1985/86 LN, although it is qualified by the Niño 3 index.

This ENSO categorization is used in the next sections, to separate the active MJO days according to the ENSO states.

3.2 ENSO-related changes in the mean state

It is convenient to recapitulate the ways the basic state (or background fields) is changed by the opposite ENSO states in which the MJO is analyzed, since they affect the intensity of MJO convective anomalies, their propagation and the teleconnections they produce. Therefore, to facilitate future discussion, some of the changes in the basic state produced by EN and LN are briefly reviewed and displayed in Fig. 2. Also shown are contours of some composite reference values for each ENSO state (purple lines), such as 28°C SST (indicating the warm pool), 225 W/m^2 OLR (indicating intense convective activity), and 25 m/s U200 contours (indicating strong zonal wind). For reference, the upper left panel shows the climatological average daily precipitation in DJF, with the white grid boxes indicating areas void of data (Fig. 2a). It also shows the main regions cited in the text: Central-east SA (CESA) and Southeast SA (SESA) (pink boxes), and the dipole action centers of the first continental intraseasonal summer precipitation variability mode, analyzed in Section 6 (blue squares). Figures 2b and 2c show the composite daily precipitation anomalies produced by EN and LN.

The ENSO-induced seasonal mean anomalies show approximately opposite signs between EN and LN events. During EN the positive equatorial central-east Pacific SST anomalies extend the warm pool and strong convection eastward to the central equatorial Pacific, while the negative west Pacific SST anomalies weaken the climatological strong convection over the Maritime Continent (Figs. 2d, 2f). Coherently, the equatorial vertical motion anomalies and the equatorial upper-level easterlies are enhanced in the central-east Pacific (Figs. 2h, 2j), and the Southern Hemisphere (SH) subtropical jet is enhanced in subtropical central Pacific (Fig. 2j), while an anomalous anticyclonic pair straddles the equator in central Pacific and a cyclonic/anticyclonic upper-level circulation pair covers subtropical SA (Fig. 2l). On the other hand, during LN the warm pool expands its latitudinal extent over the West Pacific, but reduces its longitudinal domain in the equatorial Pacific, shifting it to the southern subtropics (Fig. 2e). The convection in the West Pacific and the Maritime Continent is enhanced and also shifted to the subtropics of the Central Pacific, while the equatorial convection is weakened (Fig. 2g), coherent with the equatorial vertical motion anomalies (Fig. 2i). The climatological upper-level equatorial westerlies in central eastern Pacific are enhanced (Fig. 2k), while an anomalous cyclonic pair straddles the equator in central Pacific and an anticyclonic/cyclonic upper-level circulation pair covers subtropical SA (Fig. 2m). The longitude-height section of omega (Figs. 2h, 2i) is coherent with the SST and convection (OLR)

anomalies, displaying in EN (LN) enhanced ascending motion (subsidence) in central-east Pacific and opposite anomalies over SA, western Pacific and eastern Indian Ocean.

It is interesting to point out that for both, EN and LN, the convection is enhanced in the subtropical central-east South Pacific, although with less intensity and more to the east during EN (Figs. 2f, 2g). The features in Fig. 2 are consistent with the interannual variability of the South Pacific Convergence Zone (SPCZ) associated with ENSO (Vincent et al. 2009; Lorrey et al. 2012). In general, during EN the SPCZ is north and east of its average position and surface pressure is lower in the central South Pacific. During LN, the SPCZ usually lies south and west of its average position, consistent with a warmer SST in this region. However, an important aspect is that in both cases, EN and LN, there is more rainfall in the central subtropical South Pacific than during NT years, in EN a little more to the east than in LN.

3.3 Statistical relationship between MJO phases and ENSO states

The most numerous active MJO phases in DJF are 7 and 3 (Fig. 3a), which represent 17% and 16% of the total active MJO days, respectively (Fig. 3b). However, when the MJO phases are separated with respect to the ENSO states (Figs. 3c, 3d), it is possible to note that the higher occurrence of the MJO phase 3 is more noticeable in EN (20%), although it is also frequent in the other ENSO states, while the frequency of the MJO phase 7 is relatively greater in NT (20%) and LN (16%). It seems that the background ENSO-related anomalies influence the relative occurrence of MJO phases with similar patterns of circulation / convection anomalies. Considering the strongest anomalies of Walker circulation and convection over the equatorial eastern Indian Ocean/western Pacific Ocean and central Pacific Ocean, there are similarities between ENSO states (Fig. 2) and some MJO phases in DJF (Fig. 4, and Figs. 2, 3 in Grimm 2019). Phases 8, 1, 2, 3, which are relatively more frequent in EN (Fig. 3d), share some common features with EN: suppressed convection over the equatorial eastern Indian Ocean, Maritime Continent/western Pacific, and subtropical central-west South Pacific, while enhanced convection predominates over the equatorial central Pacific. On the other hand, phases 5, 6, 7, which are relatively more frequent in LN (Fig. 3d), display opposite common features with LN. The MJO phases that are relatively most frequent in category NT (LN) have the second highest relative frequency in LN (NT) (Fig. 3d), consistent with the fact that anomalous LN features approximately intensify NT features.

Although this study does not investigate in detail the reasons of differences in the frequency of MJO phases during different ENSO states, it is possible to hypothesize that the mean circulation and convection changes during the different states of ENSO alter the MJO related convection anomalies and moisture distribution over the equatorial region. This can change the intensity and propagation of the MJO patterns, favoring the intensity and frequency of certain MJO phases during the ENSO state with background patterns most similar to those MJO phases.

There have been analyzed 2790 days in 31 DJF seasons. From these days, 1782 (64%) were active MJO days. From the active MJO days, 404 occurred in EN, 572 in LN, and 806 in NT years. Hence, there are more active MJO days in NT years because they are more numerous (14) than EN (7) and LN (10) years.

Consequently, the samples used in the composites for NT years are larger than for EN and LN years, although the number of MJO active days per year is not very different for the different ENSO states: 57.6 (NT), 57.7 (EN) and 57.2 (LN). Therefore, the year-to-year variations of MJO activity seem to be unrelated to ENSO (Slingo et al. 1999; Hendon, Zhang and Glick 1999). Notwithstanding, there are variations of the anomalous convection and circulation patterns associated with MJO. For instance, during EN the anomalous equatorial zonal winds and convection tend to increase near and east of the Date Line and decrease in the far western Pacific (Gutzler 1991; Fink and Speth 1997). Changes in the MJO-related global patterns of convection, circulation and precipitation produced by different ENSO states are described in the next sections, with more focus on SA.

4 Mjo Impacts In Enso Neutral State

4.1 Global anomaly patterns associated with MJO in neutral years

Basic background on the MJO dynamical mechanisms, the global evolution of the MJO tropical convection and associated circulation, and the description of the MJO impacts on SA are provided in Grimm (2019). Therefore, this information will not be duplicated here, where the focus is on the ENSO modulation of MJO characteristics and impacts.

Although the global mean evolution of MJO and its impacts is well known, it is not exactly equal to the MJO evolution during ENSO NT state, since there are some nonlinear effects of ENSO on MJO that are not smoothed out in a mean over all ENSO states. Figure 4, which shows the low-level velocity potential and wind, besides OLR anomalies, for years with no ENSO signal (NT state), displays some differences with respect to Figs. 2 and 3 of Grimm (2019), computed for all years in the same period. For instance, anomalous convection over the climatological SACZ in phase 1 and winds in some places are stronger in the composites including all years, indicating that the EN and LN effects do not just combine linearly with the MJO effects. Therefore, a separate analysis for different ENSO states can be helpful in terms of subseasonal prediction and validation of models.

The general MJO patterns during an ENSO NT state are broadly consistent with the observational analysis in Grimm (2019) considering all years of the period. Notwithstanding, focusing on the phases with most extensive impacts on SA, phases 1 and 4, it is possible to detect differences. Comparing Fig. 4 (right column) with Figs. 2 and 3 in Grimm (2019), it is possible to see that in $MJO_{NT} \text{ phase 1}$ the OLR anomalies over the climatological SACZ position crossing the Brazilian coast are approximately -5.0 W/m^2 , while in the all-year composite in Grimm (2019) they reach -10.0 W/m^2 . In the equatorial NE Brazil the $MJO_{NT} \text{ phase 1}$ displays anomalous OLR -10.0 W/m^2 , while the all-year composite reaches -12.5 W/m^2 . On the other hand, in the middle of CESA the difference is small. In SESA, the $MJO_{NT} \text{ phase 1}$ presents some significant anomalies, reaching -7.5 W/m^2 , while in the all-year composite they are weaker and of opposite sign. In phase 4 there are no great differences in CESA, but in SESA the negative

anomalies in $MJO_{NT}phase4$ reach -10.0 W/m^2 , while in the all-year composite they are below -5.0 W/m^2 .

Figure 4 (left column) displays the anomalous MJO propagating low-level divergence and convergence centers and wind anomalies for NT state, for the sake of comparison with corresponding maps for EN and LN states. There are some low-level wind divergence/convergence features highlighted in subtropical central-east South Pacific, which are related with upper-level anomalous convergence/divergence anomalies (indicated by tropical OLR anomalies in Fig. 4 (right column)). They are efficient in producing the extratropical Rossby wave trains (indicated by curved arrows in Fig. 5) associated with precipitation anomalies over SA, according to Grimm (2019). There is a lag (around one phase) between the appearance of the upper-level divergence and the establishment of the wave train over SA.

Also the streamfunction anomalies at 200 hPa (Fig. 5, right column) show differences between anomaly composites for MJO phases in NT years and in all years. Grimm (2019) pointed the importance of extratropical teleconnections in contributing to the strongest and most extensive positive (negative) precipitation anomalies over SA in phases 1 (4–5) by creating a cyclonic (anticyclonic) anomaly over the subtropical continent that favored these anomalies over CESA (and opposite ones over SESA). While in $MJO_{NT}phase1$ this cyclonic center over subtropical SA responsible for the enhanced convection anomalies over CESA (and SACZ) is weak and not significant (Fig. 5, 200 hPa), in the all-year composite it is significant (Fig. 5 of Grimm 2019). Also in the Northern Hemisphere (NH) the extratropical teleconnections are affected: for instance, while in $MJO_{NT}phase7$ the extratropical teleconnection over North Pacific / North America is very weak (Fig. 5, 200 hPa), it is stronger and significant in the all-year composite (Fig. 5 of Grimm 2019). At low levels, the cyclonic anomaly over the extratropical North Pacific extends further north and in the equatorial Pacific further east in the all-years composite (Fig. 4 of Grimm 2019),

These global composites for MJO_{NT} phases will be mentioned later again, as a reference for the MJO composites in EN and LN states.

4.2 Precipitation and its extremes over SA associated with MJO in neutral years

Figure 6 shows the MJO-related precipitation behavior in SA for NT years. While the main anomaly patterns for precipitation and frequency of extreme events for NT years maintain the general characteristics of the all-years composites in Grimm (2019), some details are different, consistently with the differences already pointed out in OLR and circulation anomalies. In phase 1 of the all-years composite there are strong and significant precipitation anomalies over the climatological SACZ and a little south of it (Fig. 7 of Grimm 2019). Also the frequency of extreme events is significantly increased in this region (Fig. 8 of Grimm 2019). The composites for $MJO_{NT}phases8+1$ show weaker or no significant positive anomalies in these regions, since they are shifted northward, to central CESA and north of it

(Fig. 6), as also shown in OLR negative anomalies (Fig. 4). The same happens with less intensity to opposite anomalies in $MJO_{NT} \text{ phases } 4+5$.

5 Mjo Impacts During El Niño And La Niña States

5.1 Global anomaly patterns associated with MJO in EN and LN years

5.1.1 Why expect ENSO to influence MJO and its impacts?

There are several reasons to expect that the ENSO-related changes in the background state influence MJO and its impacts on SA. The background changes produced by opposite ENSO states in the SST warm pool, tropical convection and circulation (Fig. 2) are able to change not only the frequency of MJO phases, as already shown (Fig. 3), but also the intensity, position, size, and propagation of the MJO most notable convection features, as well as the associated circulation and teleconnections (e.g., Fink and Speth 1997; Moon, Wang and Ha 2011). For instance, the characteristic equatorial MJO eastward propagating convective anomalies are coupled with a pair of large-scale anomalous Walker cells, which can be affected by the Walker circulation changes produced by opposite ENSO states (Figs. 2h, 2i). Besides, the region with strongest MJO-related anomalous convection (subsidence), in phases 4 and 5 (8 and 1), over the Maritime Continent, around 130°E (Fig. 4 for NT years, and Fig. 2 of Grimm 2019), is also a region with strong ENSO-related convection anomalies in the West Pacific (Figs. 2f, 2g). Another region with significant MJO and ENSO-related convection anomalies is Central-East Pacific, around and east of the Date Line, where the MJO-related anomalies are of much interest to SA, since in their eastward propagation they start to weaken in this region and shift southeastward, entering a region where anomalous convection is very efficient in producing teleconnections to SA (Grimm 2019).

5.1.2 Influence of EN and LN states on MJO-related convection and circulation

The next figures show the MJO global anomalous convection and circulation patterns (Figs. 7, 8, 9, 10) during EN and LN states.

When the MJO-related anomalies are favored by oceanic and atmospheric background ENSO-related changes (Fig. 2), their intensity tends to be enhanced. Figures 7 and 8 show that in MJO phases 8, 1, 2, 3 low-level anomalous divergence and reduced convection over the eastern Indian Ocean-Maritime Continent/west Pacific and low-level anomalous convergence and enhanced convection in central Pacific are more intensified on the equatorial belt during EN than during LN. This is consistent with the EN prevalent anomalous subsidence over the former regions and dominant anomalous convection over the latter (Fig. 2 and Figs. 7 and 8). It is more visible in the anomalous OLR field (Fig. 8), and for phases 8 and 1. On the other hand, during MJO phases 5, 6, 7 the low-level anomalous convergence and enhanced convection over the eastern Indian Ocean-Maritime Continent/west Pacific and low-level anomalous

divergence and subsidence in central Pacific are more enhanced during LN, because these anomalies are also prevalent in LN (Fig. 2 and Figs. 7 and 8).

The position and size of MJO-related anomalies is also altered by ENSO opposite states. For instance, when the MJO enhanced convection is near/over the Maritime Continent, in phases 4, 5, and 6, it is more intense and extensive during LN than EN (Fig. 8), since ascending motion is enhanced in this region and the warm pool occupies a larger latitudinal extension (Figs. 2e, 2i). On the other hand, the MJO equatorial convection reaches and crosses the Date Line already in phases 5 and 6 during EN, favored by the SST and Walker circulation background conditions in this ENSO state (Fig. 2), while in NT state this only occurs in phases 6 and 7 (Figs. 4 and 8). This is consistent with the eastward shift of MJO activity during EN events reported by Hendon, Zhang and Glick (1999). On the other hand, in LN state the MJO convection is suppressed in equatorial central-east Pacific in phases 7 and 8 (Figs. 4 and 8), but appears in subtropical central-east South Pacific, which is coherent with the background in this ENSO state. As in LN the equatorial SST in the Pacific is colder east of the Date Line and the subsidence is enhanced, the tropical enhanced convection is shifted south of the equator (Fig. 2g).

In another example, when the equatorial MJO enhanced convection crosses the Date Line (phases 6 + 7), and MJO and EN (LN) anomalies have same (opposite) sign east of the Date Line, the MJO-related low-level divergence and subsidence over the equatorial northeast SA is enhanced (weakened) in $MJO_{EN} \text{ phases } 6+7$ ($MJO_{LN} \text{ phases } 6+7$) and the enhanced convection (or negative OLR) in $MJO_{EN} \text{ phases } 8+1+2$ ($MJO_{LN} \text{ phases } 8+1+2$) is weakened (increased) in this region (Fig. 8) with respect to NT state (Fig. 4). This is consistent with the effects of ENSO on the equatorial northeast SA (or eastern Amazon), shown in the upper panels of Fig. 2. In NT years, without EN or LN influence, the MJO-related subsidence observed in phases 4 + 5 + 6 over northeastern SA weakens in $MJO_{NT} \text{ phases } 6+7+8$, when the MJO convection crosses the Date Line (Fig. 4). However, during EN years there is EN-related background subsidence over northeastern SA due to the EN-related enhanced convection in central-east equatorial Pacific (Fig. 2d, 2f, 2h), which is further increased in MJO phases 6 + 7 + 8 (Fig. 8, left column). Therefore, during $MJO_{EN} \text{ phases } 6+7+8$, the subsidence over northeastern SA is stronger and stays longer than during NT or LN state (cf. Figures 4 and 8).

Some of the aspects described in the paragraphs above are also visible in Fig. 9, in which the MJO anomaly composites for the NT years are removed from the composites for EN and LN years. For instance, on the left column (EN-NT) the red ellipses show the enhancement of subsidence over the western Pacific in phases 8 and 1, when the strongest subsidence associated with the MJO coincides with the strongest subsidence associated with EN. On the other hand, on the right column (LN-NT) the blue ellipses show the enhancement of convection over the western Pacific in phases 5 and 6, when the strongest convection associated with the MJO coincides with the strongest convection associated with LN. The black ellipses will be mentioned in the next section.

5.1.3 Influence of EN and LN states on MJO propagation and teleconnections

Propagation speeds of MJO features are approximately indicated by the inclination of the arrows in Figs. 4 and 7, but are also visible in the displacement of the convection and circulation anomalies (Figs. 4, 5, 8, 10 and 11), especially in the low-level streamfunction quadrupoles, associated with the Rossby and Kelvin wave responses to the dipole of mass sink and source (heating and cooling) over the equatorial region (Matsuno 1966; reviews in Zhang 2005; Grimm 2019). The circulation anomalies are presented to facilitate discussion of the teleconnections and precipitation anomalies over SA observed in each ENSO phase. The equatorial propagation characteristics are also summarized in Fig. 12.

Since higher (lower) phase propagation speed is expected for weaker (stronger) convection (Zhang 2005; Pohl and Matthews 2007), the stronger and more extensive anomalous convection over the Maritime Continent in phase 5 during LN is consistent with much slower eastward propagation over this region (Figs. 7, 8). Besides, there is great weakening of the convection when it moves from over the Maritime Continent to the western Pacific, which is consistent with the barrier effect of the Maritime Continent (Zhang and Ling 2017). On the other hand, during EN, the anomalous convection over the Maritime Continent is weaker and does not reduce much when it moves from the Maritime Continent to the western Pacific Ocean, with higher propagation speed (Fig. 7). It crosses the Date Line in phase 6, extending further eastward in the equatorial band than in LN state (Figs. 7, 8), since the equatorial warm pool is extended further eastward during EN than during LN (Figs. 2d, 2e). On the other hand, during LN there is a quicker eastward propagation of anomalous convection on the subtropical central-eastern South Pacific, from phase 6 to 7, probably favored by the warm pool features during LN (Fig. 2e).

After the MJO convection crosses the Maritime Continent and approaches the Date Line (phase 6) (Figs. 4, 7, 8), the propagation speed over the climatologically colder ocean waters shows considerable differences between EN and LN. During EN, although stronger equatorial anomalous convection extends eastward of the Date Line, there is little propagation from phase 6 to 7 (Figs. 7, 8), and this aspect also appears in the circulation anomalies, since there is little propagation of the equatorial streamfunction anomalies over the Pacific between these phases (Figs. 10, 11). On the other hand, during LN there is no enhanced convection on the equatorial central-east Pacific, but subtropical convection is extended eastward from phase 6 to 7 into central-east South Pacific (Fig. 8). The equatorial wind perturbation propagates faster eastward and the low-level convergence and westerly winds are already strong over the eastern Pacific and SA in phase 8, while during EN they reach the maximum in phase 1 (Figs. 7, 10, 12). The same is true for the upper-level easterlies, which are stronger and propagate eastward faster over the central-east Pacific during LN than during EN (Figs. 11, 12), favoring stronger and earlier equatorial convection in the Western Hemisphere, over SA, Atlantic Ocean and Africa in phases 8 through 1 during LN.

Therefore, the tropics-tropics teleconnection between the Pacific and SA during LN state, favoring the enhancement of precipitation in northeast SA and tropical CESA, is already established in MJO_{LN} phase 8, but during EN state is only well established in MJO_{EN} phase 1 (Figs. 7, 8, 10, 11). The differences between EN and LN in the propagation of the equatorial convection anomalies across the Date Line and in the propagation of the zonal wind signal is also clear in the Hovmöller diagrams (Fig. 12). This difference

between propagation speeds in the Western Hemisphere is consistent with the reduction (increase) of the MJO phase velocity over warmer (colder) SSTs and associated with stronger (weaker) convection (Zhang 2005). Also the subtropical low-level wind convergence and associated OLR anomalies in central-east South Pacific, which are important for the extratropical teleconnection with SA, are first established in phase 7 (8) during LN (EN) (Figs. 7, 8). This subtropical convection is an important aspect related to the extratropical teleconnection between the central-east Pacific and SA (indicated schematically by the curved arrows in Figs. 5, 10, 11), since the associated upper-level divergence in this region is shown to be very efficient in triggering such teleconnection (Grimm and Silva Dias, 1995; Grimm, 2019). This region is indicated by the ellipses in Figs. 4, 7, 8. The anomalous convection in it is stronger in MJO_{EN} phases 8+1 and MJO_{LN} phases 7+8 (Fig. 8) than in MJO_{NT} phases 8+1 (Fig. 4). This is emphasized in Fig. 9, where the differences EN-NT and LN-NT are displayed. The black ellipses on the subtropical central-east South Pacific show that in these phases there is enhancement of convection in this region in both EN and LN states, starting earlier in LN than in EN, and that there is enhanced convection over CESA (and SACZ), especially in MJO_{EN} phase 1 and MJO_{LN} phase 8. The Influence Functions displayed in Fig. 11 of Grimm (2019) shows that the upper-level divergence anomalies in the subtropics of the central-east South Pacific lead to a teleconnection pattern that produces a pair anticyclonic-cyclonic circulation anomaly over the extratropics-subtropics of SA that enhances precipitation in CESA in the phases indicated above. The subtropical cyclone favors moisture flux from the Amazon into CESA (and the SACZ), where there is moisture convergence, and divergence of moisture flux from the middle/lower Parana/La Plata Basin (SESA), tending to form a convective dipole between CESA and SESA (Grimm 2019).

The extratropical teleconnection pattern is approximately indicated on the streamfunction patterns of Figs. 5, 10 and 11, in phases 8 and 1, and, with opposite sign in phase 4. It is more visible at 200 hPa, and at 850 hPa it is only indicated on the barotropic action centers. The MJO phase in which it is more clearly established varies with the ENSO state. While it is still developing in MJO_{EN} phase 8 (and strongest at MJO_{EN} phase 1), it is already fully established in MJO_{LN} phase 8 (Figs. 10 and 11). In NT years it is more consistently established with the precipitation anomalies over CESA in phase 1 (Fig. 5). The maximum enhancement of the pair extratropical anticyclone-subtropical cyclone over SA, and the strongest negative OLR anomalies in CESA, produced by the cyclonic circulation, happens earlier in the MJO cycle during LN (MJO_{LN} phase 8) with respect to EN (MJO_{EN} phase 1) and NT (MJO_{NT} phase 1). However, the highest impact on the southern edge of the SACZ in LN occurs in MJO_{LN} phase 1, associated with the subtropical cyclonic anomaly a little displaced westward, with respect to MJO_{EN} phase 1. The same advancement during LN happens to the propagation of velocity potential anomalies (Fig. 7), as well as to anomalies of precipitation and frequency of extreme events, as will be detailed later.

It is interesting to point out that there are some similar effects of EN and LN states, compared to NT state, regarding the MJO-related extratropical teleconnection from subtropical central-east South Pacific to SA. Taking phase 1 as reference (although phase 8 could also be used for the LN state), there are great differences between the MJO circulation anomalies over the continent in NT years and those in EN and LN years (cf. Figure 5 and Figs. 10 and 11). While EN and LN years show a strong anomalous pair

extratropical anticyclone-subtropical cyclone over SA (Figs. 10 and 11), in NT years it is weaker and shifted northwestward, as is also the extratropical teleconnection (Fig. 5). This teleconnection fades in MJO phase 2 (Figs. 5, 11), due to the reduction of convection in that subtropical region in South Pacific (Figs. 4, 8), weakening the positive (negative) precipitation anomalies in CESA (SESA) (next section).

Figure 13 zooms mostly the Western Hemisphere and shows OLR anomalies for MJO phases 8 and 1 in EN, NT, as well as for the difference EN-NT, to emphasize that EN increases MJO related convection anomalies in these phases in the subtropical central-east South Pacific, a region in which the upper-level divergence is very efficient in triggering the MJO extratropical teleconnection towards SA (Grimm and Silva Dias, 1995; Grimm, 2019). This figure also shows that this teleconnection pattern (visible in the 200hPa streamfunction anomalies) is much enhanced during EN, especially the cyclonic circulation pattern over subtropical SA associated with increased precipitation over CESA (and SACZ). As mentioned before and is visible in Fig. 9, and Figs. 10 and 11 when compared to Fig. 5, a similar enhancement happens during LN state.

Besides the similarity over SA, the circulation anomalies during $MJO_{EN} \text{ phase 1}$ and $MJO_{LN} \text{ phase 1}$ are also similar over the South Atlantic Ocean (Fig. 11). One of the notable features is the strong anomalous barotropic anticyclonic circulation near the southeastern coast of SA, which merges with the extratropical anticyclone over southern SA that is part of the teleconnection pattern from the Pacific. This does not appear in $MJO_{NT} \text{ phase 1}$ (Fig. 5), since it is probably partially produced by the enhanced convection in the southern edge of the SACZ during EN and LN MJO phase 1 (Figs. 4, 8).

Thus far, emphasis has been put on the circulation and convection anomalies associated with the most extensive enhanced convection over SA, in phases 8 through 2, especially phases 8 and 1. However, in phases 3 through 6, especially phases 4 and 5, the anomalous convection displays approximately opposite signs compared to that in phases 8 and 1 (Figs. 4, 8). The convection in the equatorial central Pacific and in the subtropical central-east South Pacific, important for the teleconnection towards SA, is suppressed, and the precipitation dipole is reversed on SA, enhancing the positive (negative) OLR anomalies in CESA (SESA) (Figs. 4, 8). Approximately opposite anomaly patterns have been shown in all ENSO states between phases 8 + 1 and phases 4 + 5, in convection (Figs. 4, 6, 8, 12) and circulation anomalies (Figs. 5, 10, 11), suggesting that the region of subsidence in the subtropical central-east South Pacific can trigger tropics-extratropics teleconnections, suppressing convection in the SACZ. This teleconnection is schematically represented in phase 4 (Figs. 5, 10, 11), when the wave train is best defined, especially in NT state, but in case of EN the subtropical anticyclonic circulation is strongest in phase 5 (Fig. 11).

In phases 8 and 1 the enhanced convection is strongest and shifted east in subtropical central-east South Pacific in EN with respect to LN, and therefore the teleconnection pattern towards SA is also shifted east with respect to LN, and so is the enhanced convection over SA (Figs. 8, 11) and precipitation (next section). On the other hand, enhanced subsidence over central-east subtropical South Pacific is stronger and shifted east in LN with respect to EN in phases 3 and 4, and therefore this teleconnection pattern is

stronger and slightly shifted eastward, and so is anomalous convection over SA (Figs. 8, 11). It also starts earlier, in phase 3, while in EN it is more visible in phase 4, as is more clearly seen at 850 hPa (Fig. 10).

The MJO most intense and extensive dry anomalies over SA (which peak in phases 4 and 5) take longer to be established and last longer in EN state (Fig. 8). The tropical teleconnection is slower and in EN it takes longer for the enhanced convection to move to the subtropical central-east South Pacific and reverse the convection dipole over SA, because of the slower propagation between phases 6 and 7 over the Pacific, mentioned before. During these phases in EN state positive OLR anomalies still predominate in subtropical central-east South Pacific, while in LN already negative anomalies predominate (Fig. 8). Therefore, the teleconnection pattern leading to an inverse dipole over SA starts being established in phase 8 in EN, while in this phase it is already fully established in LN. Furthermore, in the equatorial belt the enhanced subsidence during EN over the northern part of CESA also contributes to extend the dry anomalies over SA. Hence, the interannual circulation anomalies extend (shorten) the intraseasonal circulation anomalies over SA in EN (LN) during the MJO phases with dryness in CESA.

Extratropical teleconnection patterns over other regions of the globe also change between EN and LN states, as shown by Moon, Wang and Ha (2011), especially in the Northern Hemisphere, where the winter basic state favors the extratropical teleconnections triggered by tropical convection. For instance, in extratropical North Pacific, North America and North Atlantic there are noticeable differences between EN and LN in phases 7, 8, 1, such as the anomalies over northern Pacific and eastern US (Figs. 10 and 11). Yet during phases 8 and 1 the differences in Southern Hemisphere are not great, especially in the Western Hemisphere, probably because the regions with more influence on the extratropical teleconnection reaching SA are in the subtropics of central-east South Pacific and anomalous MJO convection is not that different between EN and LN in those regions.

Some features pointed out thus far in the equatorial belt are visible and summarized in the MJO Hovmoller diagrams for the three ENSO states. The quicker and more eastward propagation of the OLR anomalies over the Indian Ocean/western Pacific in EN (Fig. 12b) than LN (Fig. 12c) is clearly visible in the lower slope of the OLR diagram for EN in this range of longitudes (between 60°E-120°E). The equatorial convection stays longer a little east of the Date Line during EN (phases 6 and 7), which is coherent with the anomalous Walker circulation with ascending motion over this region, and then extends eastward (and southward) till 120°W (cf. Figures 12b and 8 left). Yet in LN the equatorial propagation of convection is slower till a little west of the Date Line (although it extends southeastward in the subtropics) (cf. Figures 12c and 8 right). Therefore, the equatorial propagation of anomalous convection ends near the Date Line in LN, also coherent with the Walker circulation basic state in this category. The equatorial enhanced convection only reappears over equatorial SA in phases 8-1-2, and is stronger during LN than EN (cf. Figures 12b, 12c and 8). The MJO eastward propagation over colder SSTs in the central-eastern equatorial Pacific is better represented in the upper-level zonal winds (Figs. 12g, 12h, 12i). They have a higher phase velocity since they are associated with free Kelvin waves uncoupled with convection and quicker/stronger for LN than for EN. They propagate faster and are more intense in the region near SA (a little east of 120°W) during LN, when SSTs are colder, there is no deep convection over the eastern

Pacific, and the convection over tropical SA is stronger. The anomalous positive SSTs over central-eastern equatorial Pacific in EN decrease the phase velocity of the MJO (Figs. 12e, 12h, between 180°W-160°W, phases 6–7), slowing its convection across the region (Fig. 8), and causing a delay in the inversion of the intraseasonal dipole over SA until MJO_{EN} phase 7.

5.2 Precipitation and its extremes over SA associated with MJO in EN and LN states

In the previous section, the global patterns of MJO convection (OLR anomalies) and circulation were analyzed. In this section a more detailed and reliable picture of the South American anomalies of precipitation and frequency of extreme events, obtained from rain gauge data, is presented. The focus is on the differences between MJO impacts in EN and LN states because the differences between the composite anomalies for NT years and all years have been briefly described in section 4.2, and the main mechanisms behind these anomalies are explained in Grimm (2019).

5.2.1 Precipitation anomalies

As in Grimm (2019), it is convenient to start the analysis from phase 7, when the anomalous precipitation dipole between CESA and SESA starts inverting polarity over SA in NT years, entering the phase with strongest precipitation in CESA (Fig. 6). In EN state, the dipole reversal is delayed compared to LN and NT years, as already seen in the OLR anomaly composites (Figs. 4, 8). While in NT and LN the CESA-SESA dipolar characteristic is lost in phase 7, it is still clear in the EN state, in which the transition takes place in phase 8 (Fig. 14) and the highest difference between the dipole centers happens in phase 1, fading in phase 2. In LN the transition starts in phase 7, the highest difference lasts from phase 8 through phase 1, and the dipole is still discernible in phase 2. Therefore, the transition from maximum negative anomalies to maximum positive anomalies in CESA happens later and this polarity lasts for a shorter time in EN than in LN, making the precipitation dipole antisymmetric with respect to the time distribution of its phases. While the positive precipitation anomalies during EN are strong only over CESA, during LN they also extend over Central SA and other parts of the Amazon. During LN, they are stronger over northern CESA in phase 8 and enhanced in its southern part in phase 1 (Fig. 14). These differences are consistent with the different EN and LN basic states and circulation anomalies, and with the extratropical teleconnection eastward shift in EN and westward shift in LN, discussed previously.

Hence, the most significant positive precipitation anomalies in CESA happen in MJO_{EN} phase 1 and MJO_{LN} phase 8. Moreover, the spatial rainfall distribution in CESA is different in this enhanced precipitation period during EN, LN and NT years. In EN (Fig. 14), the positive precipitation anomalies are weak in phase 8, but very prominent in phase 1, extending from the SACZ region, where they are supported by the extratropical teleconnection from the subtropical central-east South Pacific, to NE Brazil, where they are supported by strong westerly wind anomalies at lower levels, associated with Kelvin wave tropical teleconnection (Fig. 7). The contribution of the filtered precipitation anomalies related to the MJO in EN years reaches more than 5 mm/day, which is equivalent to 50% of the daily precipitation

climatology in DJF over extensive regions of the SA monsoon core region in central SA (Fig. 2a). In $MJO_{LN}phase1$, the positive precipitation anomalies are enhanced over central Brazil and in the southern edge of the SACZ, with significant positive precipitation anomalies extending beyond $20^{\circ}S$, reaching the northern part of SESA (Fig. 14).

The most intense positive precipitation anomalies over CESA are observed in $MJO_{EN}phase1$, from SACZ to northern CESA and Northeast Brazil (Fig. 14). On the other hand, the negative precipitation anomalies in SESA are stronger in $MJO_{LN}phases8+1$ (Fig. 14) and weaker in $MJO_{EN}phases8+1$, because of the favorable conditions to subsidence in SESA during LN and enhanced precipitation during EN (Grimm 2003, 2004).

When the positive precipitation anomalies retract towards NE Brazil in phase 2, they remain significant in NT years (Fig. 6) and LN years (Fig. 14), but fade in EN years (Fig. 14), due to the unfavorable EN basic state with subsidence over Northeast Brazil. The OLR anomalies show that when convection is enhanced (weakened) in central equatorial Pacific due to combined effect of EN (LN) and MJO the enhanced convection over the equatorial northeast SA in phases 8, 1 and 2 is stronger in LN than in EN (Fig. 8).

Following the MJO phases 4, 5 and 6, when the precipitation anomalies are reversed over CESA and SESA, in EN the negative precipitation anomalies in CESA are enhanced between phases 4 and 7, while in LN they are most enhanced in phases 4 and 5, especially the latter. ENSO plays a role in enhancing the strongest MJO precipitation anomalies in CESA. At the same time, it influences the precipitation anomalies in SESA, where the positive precipitation anomalies are more frequent in EN than in LN (Fig. 14), which is coherent with the ENSO effect on SESA (Grimm 2003; 2004). In $MJO_{EN}phases3-7$ only in $MJO_{EN}phase5$ negative anomalies occupy part of southern Brazil, because the subtropical anticyclonic anomaly in $MJO_{EN}phase5$ is shifted south, but there are still positive anomalies in the southern part of SESA (Fig. 14) (Figs. 5, 10, 11). Yet only in $MJO_{LN}phases3-5$ there are significant positive anomalies over SESA, coherent with the LN effect on this region (Fig. 14).

5.2.2 Extreme precipitation frequency

As the ENSO and the MJO are known to increase significantly the frequency of extreme events on SA (Grimm and Tedeschi 2009; Hirata and Grimm 2015; Grimm 2019), it is important to verify how the ENSO states modulate the MJO impacts on extreme events. In the previous section it was shown that ENSO impacts strongly on average daily precipitation anomalies in certain MJO phases. Therefore, it is relevant to check if the ENSO-MJO effect on the frequency of extreme events is consistent with the impact on the daily mean precipitation, since the social impact of changes in extremes is more dramatic than changes in average precipitation. Here this analysis is exhibited in detail using observed rain gauge data, since gridded datasets underestimate extreme precipitation events on SA in areas much affected by the MJO (Hirata and Grimm, 2018), highlighting the importance of this analysis.

Figures 6 and 15 exhibit the ratio between the probability of occurrence of extreme precipitation events for each combination of ENSO state and MJO phase and the mean probability. Although the effect on the

frequency of extremes follows approximately the effect on daily precipitation (Figs. 5 and 14), there are instances in which the effect on the extremes is strong, but does not affect the average daily precipitation significantly, and vice-versa.

During EN, this happens in $MJO_{EN}phase2$, when changes in the average daily precipitation display little significance (Fig. 14) while extremes are impacted significantly over CESA and SESA (Fig. 15). On the other hand, in $MJO_{EN}phases5+6$ the effect on the extremes is weaker than over the average rainfall. In $MJO_{EN}phase1$ and 3 there is consistency between these effects, and the EN influence is responsible for the strongest and most extensive MJO impacts on CESA (and SACZ) in phase 1 and SESA in phase 3 (Figs. 14, 15), much stronger than in NT (Fig. 6). The streamfunction anomalies for $MJO_{EN}phase1$ (Fig. 11) show favorable anomalies to enhance the circulation associated with extremes in the SACZ (cf. Figure 11 with Fig. 13 of Tedeschi, Grimm and Cavalcanti 2015), while phase 3 shows a reversed dipole over SA, which favors higher precipitation in SESA. The frequency of extreme rainfall events in $MJO_{EN}phase1$ more than doubles over the SACZ, the eastern edge of monsoon core region, and the NE Brazil, very populated regions of Brazil.

During LN, in $MJO_{LN}phase6$ the effect on the extremes in CESA is stronger than on the average rainfall, except on the southern edge of the SACZ (cf. Figures 14 and 15). Another example is the extreme northwest of SA in $MJO_{LN}phases8+1$, since in $MJO_{LN}phase8$ the average rainfall over CESA increases more significantly and extensively than its extreme events. During $MJO_{LN}phase1$, as also happens during EN, there is consistent increase in rainfall and its extreme events in the SACZ, especially its southern edge, corroborating Hirata and Grimm (2015), who found an increase in extreme events under the same scenario in the southeast Brazilian coast. Albeit the frequency of extreme events doubles, this region is smaller and to the south of that observed in $MJO_{EN}phase1$ (Fig. 15).

The EN state contributes significantly to increase the frequency of extreme events in SESA during $MJO_{EN}phases2-8$ with respect to states LN and NT, with only a weakening in phase 5. In some cases there is increase even in phases when in LN and NT there is decrease of extreme events in SESA, such as phases 7 and 8 (Figs. 15 and 6). The enhancement of the occurrence of extreme events by factors greater than 2.0 during several MJO phases in EN occurs in vast regions of SESA, as Southern Brazil, Paraguay, Uruguay and Argentina, corroborating Hirata and Grimm (2015), who found similar results over the La Plata Basin. Hence, the EN modulates MJO impacts on extreme events in SESA, enhancing and prolonging these impacts, because of the EN enhancement of anomalous Hadley circulation and regional circulation that favor the precipitation in this region (Grimm, Barros and Doyle, 2000; Grimm, 2003).

Regarding the LN state, coherently with the LN teleconnections to SESA, it causes a decrease of the number of extreme events in SESA with respect to NT (cf. Figures 15 and 6) in $MJO_{LN}phases2-8$, even when average precipitation is increased, with only a weakening in phase 5, but it is less intense than the increase produced by EN.

The changes in the frequency of extreme events during MJO phases in NT years (Fig. 6) resemble the patterns described by Grimm (2019) (its Fig. 8) using all the years in the same period, with the greatest difference residing in phases 1 and 5. In NT years (Fig. 6) the dominant changes of the frequency of extreme events in CESA are limited to north of 15°S, with insignificant changes or even isolated opposite changes over the SACZ. Yet when using all years, the dominant changes extend southward, to the SACZ region. This means that both, EN and LN years contribute to change the frequency of extreme events in this region (as was already reported for the average precipitation), which is clearly visible in Fig. 15. This corroborates Hirata and Grimm (2015), who identified a weakening of the extreme events on intraseasonal scales in the SE Brazilian coast during neutral ENSO years.

The highest impact on the frequency of extreme events in SESA in NT years takes place in phase 4, followed by phase 3, consistently with the most intense precipitation anomalies (Fig. 6). In a composite using all years, Grimm (2019) emphasizes the increase in the frequency of extreme events in phase 3 over SESA, which has a more significant contribution from EN (Fig. 15) than NT (Fig. 6). Hence, the highest growth in the frequency of extreme events in SESA happens in $MJO_{EN} \text{ phase 3}$ (Fig. 15), while in NT it occurs in phase 4 (Fig. 6).

The strongest modulation of MJO impacts on extremes happens during the EN state, probably because the LN state represents an enhancement of climatological conditions over the Pacific.

6 Enso Modulation Of The Mjo Impact On The First Intraseasonal Precipitation Variability Mode In Sa

There is a dipolar mode of monsoon precipitation intraseasonal variability in SA featuring opposite anomalies between CESA and SESA, which is present in all intraseasonal time scales (Grimm 2019, its Fig. 9, REOF1, partially adapted in Fig. 16, upper left panel, in order to define the areas of the action centers of this dipole). This intraseasonal dipole oscillation over SA has been detected long ago (e. g., Casarin and Kousky 1986; Nogués-Paegle and Mo 1997; Diaz and Aceituno 2003). Recently the potential of its subseasonal prediction was assessed (Grimm, Hakoyama and Scheibe 2021), since the major MJO impacts on SA daily precipitation project strongly on this mode, as shown for $MJO_{NT} \text{ phase 4}$ in Fig. 16 (upper right panel).

Since both action centers of this dipolar oscillation are in very populated regions, with great agricultural activity and hydroelectric energy generation, it is interesting to analyze how this mode is affected by ENSO modulation of the MJO impacts on SA monsoon precipitation. Figure 16 (bottom panels) represents the DJF average daily precipitation anomalies stratified by ENSO state and MJO phase over the regions representing the northern and southern centers of this mode, in CESA and SESA, respectively (see also Fig. 2a).

It is worth emphasizing that the northern center of this dipole (in CESA) displays much stronger intraseasonal variability than the southern one (in SESA). On the other hand, the ENSO impact in summer

is stronger over SESA than over CESA (Figs. 2b, 2c), as shown by the interannual precipitation mode associated with ENSO (Grimm and Zilli 2009; Grimm 2011). This is coherent with the fact that the differences between the curves for EN and LN in Fig. 16 are larger for SESA than for CESA and that for SESA the prevalent differences with respect to NT years are positive for EN years and negative for LN years in Fig. 16, while for CESA there is no obvious preference.

This analysis shows results coherent with the observed changes in precipitation discussed in section 5.2.1. Considering the strongest Walker circulation and convection anomalies over the equatorial eastern Indian Ocean/western Pacific Ocean and the central/eastern Pacific Ocean associated with ENSO and MJO, the MJO phases that most project on the ENSO states in DJF are MJO8 + 1 (onto EN state) and MJO4 + 5 (onto LN state) (cf. Figures 2 and 4). Therefore, we would expect the anomalous convection and circulation in $MJO_{EN} \text{ phases } 8+1$ and $MJO_{LN} \text{ phases } 4+5$ to be reinforced in EN and LN, respectively. As there is a lag between forcing and precipitation response, strongest enhancement of the MJO-related anomalies in CESA would be expected in $MJO_{EN} \text{ phase } 1$ and $MJO_{LN} \text{ phase } 5$. This is confirmed in Fig. 14 and Fig. 16. On the other hand, anomalies in CESA would be expected to weaken in $MJO_{EN} \text{ phase } 5$ and $MJO_{LN} \text{ phase } 1$, with respect to the opposite ENSO state. These reduced anomalies are reflected in Fig. 16 (bottom left panel). Comparison of the anomalies in Fig. 14 with those in Fig. 6 shows that really the CESA anomalies are weakened in $MJO_{EN} \text{ phase } 5$ and $MJO_{LN} \text{ phase } 1$ with respect to the corresponding MJO phases in the opposite ENSO state, with the exception of the anomalies in the southern edge of the SACZ, which are enhanced in both EN and LN states, due to extratropical teleconnections triggered by subtropical convective anomalies in central-east South Pacific, as mentioned in section 5.1.3. This enhancement of SACZ in MJO phase 1 during both EN and LN probably represents a nonlinear ENSO effect on MJO anomalies over SA.

Although the evolution through the MJO phases of the average daily precipitation anomalies over SESA (Fig. 16 bottom right panel) is approximately opposite to that over CESA (Fig. 16 bottom left panel), there is a larger influence of EN in increasing precipitation with respect to NT years in this region and of LN in decreasing it. The greatest deviation from this behavior occurs in phase 5, when the anomalies in SESA during EN are greatly reduced in relation to those obtained in LN (and even NT), which is consistent with the fact that the phase 5 pattern of MJO is weakened in EN and strengthened in LN. This is also consistent with the fact that also in CESA the anomalies in $MJO_{EN} \text{ phase } 5$ the anomalies are weaker than in $MJO_{LN} \text{ phase } 5$. Since the SESA center of the dipole is a subtropical/extratropical region, the influence of MJO is not so direct as in CESA, and there are different sources of variability, sometimes with contrasting effects: extratropical teleconnections produced by Rossby waves, anomalous Hadley circulation, the subsidence associated with the enhanced convection in the CESA center of the dipole, which happens to southwest of the enhanced convection (Gandu and Silva Dias 1998).

The MJO drives more precipitation variability in ENSO than in NT years, and stronger in EN than in LN. The amplitude of variation in EN is around 5.0 mm/day in the CESA center and 1.5 mm/day in the SESA center, while during LN the amplitudes are, respectively, 4.0 mm/day and 2.3 mm/day (Fig. 16). In CESA,

the EN state is able to more strongly modulate MJO-related rainfall anomalies by increasing the maximum (phase 1) during the wet period rather than by reducing the minimum (phase 4) during the dry period, although this dry period in EN state is more persistent than in NT state. On the other hand, the opposite occurs during LN state, with strongest reduction of the minimum in the dry period (phase 5) and weaker increase in the wet period (phase 8) (Fig. 16).

7 Conclusions

This investigation has addressed the modulation of the MJO and its main impacts on SA precipitation by the ENSO states (EN, LN, NT) in observational datasets. Although the MJO activity, expressed by the intraseasonal variance of some fields, does not show great connection with ENSO (e.g., Hendon, Zhang and Glick 1999), the ENSO modulation of the MJO-related anomalies can produce significant changes in their impacts over SA. The equatorial eastward propagating MJO convective anomalies, coupled with a pair of large-scale anomalous Walker cells, are affected by the significant changes in the basic Walker circulation produced by the EN and LN states. Furthermore, the background ENSO-related SST, convection and circulation anomalies (Fig. 2) influence the relative occurrence of MJO phases (Fig. 3), the eastward MJO propagation (Figs. 4, 7, 12), the position and intensity of the MJO-related convection (Figs. 4, 8), the MJO-related teleconnections (Figs. 5, 9, 11), and the impacts on precipitation and extremes over SA (Figs. 6, 14, 15, 16).

It is worth reminding that the results do not simply show the added anomalies produced by ENSO and MJO. The anomalies displayed are filtered in the 20–90 day band. Therefore, they show the effect of the ENSO states on the MJO itself and its impacts, since the basic state in which the MJO develops is altered by these states (background SST warm pool, circulation, most intense tropical convection (Fig. 2)). Changes in these impacts in opposite ENSO states with respect to the NT state are not always opposite, indicating the existence of both linear and nonlinear effects.

The different propagation speeds over the Indian Ocean and the Pacific Ocean observed in Figs. 4, 7 and 12 have been explained in previous studies as a change in the phase speed of the equatorial Kelvin wave component of the MJO in a moist convective regime as in the Indian Ocean or in a dry regime (as over the central-east Pacific) (e.g., Zhang 2005; Pohl and Matthews 2007; Wei and Ren 2019). The changes in the MJO propagation speed over the Maritime Continent-western Pacific sector between EN and LN states may be due to the fact that during EN (LN), conditions over this area are drier (wetter) than normal, related to the suppression (enhancement) of mean convection there. Hence, there will be a weak “dry” regime (enhanced moist convective regime) over the sector, and the MJO would be expected to speed up (slow down) there in EN (LN), as observed. On the other hand, over the central-eastern Pacific, the MJO propagation speed decreases (increases) in EN (LN) due to warmer (colder) SSTs (Zhang 2005). The wind perturbation propagates faster eastward and the low-level convergence and westerly winds are already strong over the eastern Pacific and SA in MJO phase 8 during LN, while during EN they reach the maximum in phase 1 (Figs. 7, 10, 12). The same is true for the upper-level easterlies, which are stronger and propagate eastward faster over the central-east Pacific during LN than during EN (Figs. 11, 12). This

effect may be responsible for the earlier appearance of anomalous convection over SA in LN (phase 8) than in EN (phase 1) (Figs. 8, 12).

Concerning MJO-related convection, the main features of MJO phases that are similar to characteristics of the EN and LN states are enhanced during these states, as shown by the peaks of enhanced convection over the Maritime Continent in phase 5 during LN and enhanced convection in central equatorial Pacific in phase 1 during EN. Besides, the influence of ENSO opposite background states can also shift, extend, reduce, enhance or weaken MJO-related anomalous patterns. For instance, over northeast SA, the MJO-related anomalous subsidence and dryness that occurs mainly in phases 5 and 6 is enhanced during EN and extended to phase 7, while anomalous wetness in phases 1 and 2 is reduced, thanks to the EN background anomalies of Walker circulation subsidence over that region. During the LN state, the opposite occurs (cf. Figures 4 and 8).

ENSO can modify the MJO-rainfall relationship in SA not only because it modifies the MJO characteristics regarding convective anomalies and their propagation, but also because it creates different basic states through which the perturbations propagate toward SA, affecting the physical mechanisms by which the MJO influences rainfall variability in SA.

The anomalous precipitation composites for MJO phases in NT ENSO conditions (Fig. 6) show some differences with respect to the composites for all years in Grimm (2019) (its Fig. 7). This indicates that ENSO enhances some aspects, with EN and LN favoring anomalies with same sign in important regions and MJO phases. The most prominent example refers to the anomalies in southern CESA, over the SACZ. CESA displays the most intense and extensive anomalies, positive in phases 8 + 1 and negative in phases 4 + 5 (Fig. 14). It is noticeable that the NT precipitation anomalies are weaker over its southern part, over the SACZ and its southern edge (Fig. 6). Figure 14 shows that in both EN and LN states there is enhanced precipitation in this region in phases 8 + 1 and reduced precipitation in phases 4 + 5 with respect to NT state. Since Grimm (2019) showed that an important part of these anomalies in southern CESA is due to tropics-extratropics teleconnections with the subtropical central-east South Pacific, and both ENSO states provide forcing in this region efficient in producing this teleconnection, it seems that nonlinear effects are acting and ENSO has an important role in this regard.

The slower (faster) eastward propagation of the MJO signal over the equatorial central-eastern Pacific, probably due to warmer (colder) SSTs and enhancement (suppression) of convection in this region during EN (LN) (Figs. 2, 7 and 12), delays (anticipates) the MJO phase in which there is inversion of the intraseasonal precipitation dipole over CESA in EN (LN) (Fig. 16), making the distribution of positive and negative precipitation anomalies in CESA less (more) symmetric in EN (LN) than in NT. This effect is more noticeable in the second half of the MJO cycle (phases, 6, 7, 8), since in this period there is the strongest difference between EN and LN equatorial anomalous convection in central-east Pacific, between 180°-120°W (Fig. 8). The decreased (increased) MJO phase velocity leads to the peak of the tropics-tropics teleconnections between the central-eastern equatorial Pacific and SA in MJO_{LN}phase8, while it happens later in MJO_{EN}phase1 (Figs. 10, 11). Besides, since the different EN/LN OLR background

states affect the enhanced MJO convection over the subtropical central-eastern South Pacific, favoring it in MJO_{LN} phases 7+8 and, a little further east, in MJO_{EN} phases 8+1 (Fig. 8), these differences affect the evolution, strength, and propagation of the tropics-extratropics teleconnections to SA in ENSO years (Fig. 11). They are stronger one phase later and are shifted east in MJO_{EN} phases 8+1 with respect to MJO_{LN} phases 8+1.

Therefore, the strongest impact over CESA in SA is advanced by one phase in LN with respect to EN, since both, the tropics-tropics and the tropics-extratropics teleconnections that connect the MJO to SA are established one phase before in LN (Figs. 10 and 11). Notwithstanding, the impact on subtropical CESA (and in the SACZ) rainfall and its extremes is still strong in MJO_{LN} phase 1, being a little displaced westward in MJO_{LN} phases 8+1 with respect to MJO_{EN} phases 8+1 (Figs. 8, 10, 11, 14).

Observations also show that MJO_{EN} phase 4 and MJO_{LN} phase 4 favor suppressed MJO convection in the central-eastern subtropical South Pacific (Fig. 8), stronger and a little further east in MJO_{LN} phase 4 than MJO_{EN} phase 4. It shifts the tropics-extratropics teleconnections to SA eastward in MJO_{LN} phase 4 with respect to MJO_{EN} phase 4 (Fig. 11). This behavior is analogous to the teleconnection wave train displaced eastwards in MJO_{EN} phases 8+1 with respect to MJO_{LN} phases 8+1 due to enhanced convection over the central-eastern subtropical South Pacific stronger and more to the east in MJO_{EN} phases 8+1 than MJO_{LN} phases 7+8. Therefore, the ENSO seems to modulate the MJO teleconnections to SA in complex ways due to its widespread influence on both the basic state and the MJO convective anomalies.

The ENSO-driven changes in the MJO impacts on SA are more significant and extensive in the frequency of extreme events than in the precipitation anomalies. It could be argued that the frequency of extreme events (Fig. 15) is extensively and significantly much enhanced (or reduced) with respect to NT (Fig. 6) in regions where the effects of both ENSO and MJO contribute to enhance (or reduce) them. The strongest modulation of MJO impacts on extremes happens during the EN state, probably because it represents a stronger deviation from the climatology, since the LN state represents an enhancement of climatological conditions over the Pacific. The most striking impacts increase more than twice the frequency of extreme events in CESA during MJO_{EN} phase 1 and in SESA during MJO_{EN} phase 3. Since these are highly populated regions in SA, and summer is the rainy season in CESA and part of SESA, it is relevant to know these effects.

Additional ongoing research is focused on linear and nonlinear ENSO effects on MJO and analysis of models' skill in simulating the observed results, since they are important for subseasonal prediction during the summer monsoon (Grimm, Hakoyama and Scheibe 2021).

Declarations

Acknowledgements:

A. M. G. received financial support from the National Council for Scientific and Technological Development (CNPq-Brazil) and L. G. F. was partially supported by Coordination for the Improvement of Higher Education Personnel (CAPES-Brazil).

Funding:

A. M. G. received financial support from the National Council for Scientific and Technological Development (CNPq-Brazil) and L. G. F. was partially supported by Coordination for the Improvement of Higher Education Personnel (CAPES-Brazil).

Conflicts of interest/Competing interests:

There are no conflicts of interest.

Availability of data and material:

The data used in this research are available at the websites of the institutions cited in the text.

Code availability:

Not applicable.

Authors' contributions:

Both authors contributed equally to the study.

References

1. Aceituno P (1988) On the Functioning of the Southern Oscillation in the South American Sector. Part I: Surface Climate. *Monthly Weather Review* 116:505–524. [https://doi.org/10.1175/1520-0493\(1988\)116<0505:OTFOTS>2.0.CO;2](https://doi.org/10.1175/1520-0493(1988)116<0505:OTFOTS>2.0.CO;2)
2. Alvarez MS, Vera CS, Kiladis GN, Liebmann B (2015) Influence of the Madden Julian Oscillation on precipitation and surface air temperature in South America. *Clim Dyn* 46:245–262. <https://doi.org/10.1007/s00382-015-2581-6>
3. Arcodia MC, Kirtman BP, Siqueira LSP (2020) How MJO teleconnections and ENSO interference impacts U.S. precipitation. *J Clim* 33:4621–4640. <https://doi.org/10.1175/JCLI-D-19-0448.1>
4. Cai W, McPhaden MJ, Grimm AM et al (2020) Climate impacts of the El Niño–Southern Oscillation on South America. *Nature Reviews Earth & Environment* 1:215–231. <https://doi.org/10.1038/s43017-020-0040-3>
5. Carvalho LMV, Jones C, Liebmann B (2004) The South Atlantic Convergence Zone: Intensity, Form, Persistence, and Relationships with Intraseasonal to Interannual Activity and Extreme Rainfall. *J Clim* 17:88–108. [https://doi.org/10.1175/1520-0442\(2004\)017<0088:TSACZI>2.0.CO;2](https://doi.org/10.1175/1520-0442(2004)017<0088:TSACZI>2.0.CO;2)

6. Casarin DP, Kousky VE (1986) Precipitation anomalies in Southern Brazil and variations of the atmospheric circulation. *Rev Bras Meteor* 1:83–90
7. Dawson A (2016) Windspharm: A High-Level Library for Global Wind Field Computations Using Spherical Harmonics. *Journal of Open Research Software* 4. <https://doi.org/10.5334/jors.129>
8. Dee DP et al (2011) The ERA-Interim reanalysis: configuration and performance of the data assimilation system. *Q J Roy Meteor Soc* 137:553–597. <https://doi.org/10.1002/qj.828>
9. Díaz A, Aceituno P (2003) Atmospheric Circulation Anomalies during Episodes of Enhanced and Reduced Convective Cloudiness over Uruguay. *J Clim* 16:3171–3185. [https://doi.org/10.1175/1520-0442\(2003\)016<3171:ACADEO>2.0.CO;2](https://doi.org/10.1175/1520-0442(2003)016<3171:ACADEO>2.0.CO;2)
10. Duchon CE (1979) Lanczos Filtering in One and Two Dimensions. *J Appl Meteor* 18:1016–1022. [https://doi.org/10.1175/1520-0450\(1979\)018<1016:LFIOAT>2.0.CO;2](https://doi.org/10.1175/1520-0450(1979)018<1016:LFIOAT>2.0.CO;2)
11. Fink A, Speth P (1997) Some potential forcing mechanisms of the year-to-year variability of the tropical convection and its intraseasonal (25-70-day) variability. *Int J Climatol* 17:1513–1534. [https://doi.org/10.1002/\(SICI\)1097-0088\(19971130\)17:14<1513::AID-JOC210>3.0.CO;2-U](https://doi.org/10.1002/(SICI)1097-0088(19971130)17:14<1513::AID-JOC210>3.0.CO;2-U)
12. Gandu AW, Silva Dias PL (2018) Impact of tropical heat sources on the South American tropospheric upper circulation and subsidence. *J Geophys Res* 103:6001–6015. <https://doi.org/10.1029/97JD03114>
13. Ghelani RPS et al (2017) Joint Modulation of Intraseasonal Rainfall in Tropical Australia by the Madden-Julian Oscillation and El Niño-Southern Oscillation. *Geophys Res Lett* 44:10754–10761. <https://doi.org/10.1002/2017GL075452>
14. Grimm AM (2003) The El Niño Impact on the Summer Monsoon in Brazil: Regional Processes versus Remote Influences. *J Clim* 16:263–280. [https://doi.org/10.1175/1520-0442\(2003\)016<0263:TENIOT>2.0.CO;2](https://doi.org/10.1175/1520-0442(2003)016<0263:TENIOT>2.0.CO;2)
15. Grimm AM (2004) How do La Niña events disturb the summer monsoon system in Brazil? *Clim Dyn* 22:123–138. <https://doi.org/10.1007/s00382-003-0368-7>
16. Grimm AM (2011) Interannual climate variability in South America: impacts on seasonal precipitation, extreme events, and possible effects of climate change. *Stoch Environ Res Risk Assess*, 25:537–554. <https://doi.org/10.1007/s00477-010-0420-1>
17. Grimm AM (2018) South American Monsoon and its Extremes. In: Vuruputur VJ, Sukhatme R, Murtugudde R, Roca (eds) *Tropical Extremes: Natural Variability and Trends*, Elsevier, Amsterdam, pp 51–93. <https://doi.org/10.1016/B978-0-12-809248-4.00003-0>
18. Grimm AM (2019) Madden–Julian Oscillation impacts on South American summer monsoon season: precipitation anomalies, extreme events, teleconnections, and role in the MJO cycle. *Clim Dyn* 53:907–932. <https://doi.org/10.1007/s00382-019-04622-6>
19. Grimm AM, Ambrizzi T (2009) Teleconnections into South America from the Tropics and Extratropics on Interannual and Intraseasonal timescales. In: Vimeux F, Sylvestre F, Khodri (eds) *M. Past climate*

- variability in South America and Surrounding Regions: from the last glacial maximum to the Holocene, 14^a ed. Springer, USA, pp 159–191
20. Grimm AM, Barros VR, Doyle ME (2000) Climate Variability in Southern South America associated with El Nino and La Nina events. *J Clim* 13:35–58. [https://doi.org/10.1175/1520-0442\(2000\)013<0035:CVISSA>2.0.CO;2](https://doi.org/10.1175/1520-0442(2000)013<0035:CVISSA>2.0.CO;2)
 21. Grimm AM, Ferraz SET, and Gomes J (1998) Precipitation Anomalies in Southern Brazil Associated with El Nino and La Nina Events. *J Clim* 11:2863–2880. [https://doi.org/10.1175/1520-0442\(1998\)011<2863:PAISBA>2.0.CO;2](https://doi.org/10.1175/1520-0442(1998)011<2863:PAISBA>2.0.CO;2)
 22. Grimm AM, Hakoyama LR, Scheibe LA (2021) Active and break phases of the South American summer monsoon: MJO influence and subseasonal prediction. *Clim Dyn* 56:3603–3624. <https://doi.org/10.1007/s00382-021-05658-3>
 23. Grimm AM, Pal JS, Giorgi F (2007) Connection between Spring Conditions and Peak Summer Monsoon Rainfall in South America: Role of Soil Moisture, Surface Temperature, and Topography in Eastern Brazil. *J Clim* 20:5929–5945. <https://doi.org/10.1175/2007JCLI1684.1>
 24. Grimm AM, Saboia JPJ (2015) Interdecadal Variability of the South American Precipitation in the Monsoon Season. *J Clim* 28:755–775. <https://doi.org/10.1175/JCLI-D-14-00046.1>
 25. Grimm AM, Silva Dias PL (1995) Analysis of tropical-extratropical interactions with influence functions of a barotropic model. *J Atmos Sci* 52:3538–3555. [https://doi.org/10.1175/1520-0469\(1995\)052<3538:AOTIWI>2.0.CO;2](https://doi.org/10.1175/1520-0469(1995)052<3538:AOTIWI>2.0.CO;2)
 26. Grimm AM, Tedeschi RG (2009) ENSO and Extreme Rainfall Events in South America. *J Clim* 22:1589–1609. <https://doi.org/10.1175/2008JCLI2429.1>
 27. Grimm AM, Zilli MT (2009) Interannual Variability and Seasonal Evolution of Summer Monsoon Rainfall in South America. *J Clim* 22:2257–2275. <https://doi.org/10.1175/2008JCLI2345.1>
 28. Gutzler DS (1991) Interannual Fluctuations of Intraseasonal Variance of Near- Equatorial Zonal Winds. *J Geophys Res* 96:3173–3185. <https://doi.org/10.1029/90jd01831>
 29. Hendon HH, Wheeler MC, Zhang C (2007) Seasonal Dependence of the MJO-ENSO Relationship. *J Clim* 20:531–543. <https://doi.org/10.1175/JCLI4003.1>
 30. Hendon HH, Zhang C, Glick JD (1999) Interannual Variation of the Madden-Julian Oscillation during Austral Summer. *J Clim* 12:2538–2550. [https://doi.org/10.1175/1520-0442\(1999\)012<2538:ivotmj>2.0.co;2](https://doi.org/10.1175/1520-0442(1999)012<2538:ivotmj>2.0.co;2)
 31. Hirata FE, Grimm AM (2015) The role of synoptic and intraseasonal anomalies in the life cycle of summer rainfall extremes over South America. *Clim Dyn* 46:3041–3055. <https://doi.org/10.1007/s00382-015-2751-6>
 32. Hirata FE, Grimm AM (2018) Extended-range prediction of South Atlantic convergence zone rainfall with calibrated CFSv2 reforecast. *Clim Dyn* 50:3699–3710. <https://doi.org/10.1007/s00382-017-3836-1>
 33. Kalnay E et al (1996) The NCEP/NCAR 40-year reanalysis project. *Bull Am Meteor Soc* 77: 437–471. [https://doi.org/10.1175/1520-0477\(1996\)077<0437:TNYRP>2.0.CO;2](https://doi.org/10.1175/1520-0477(1996)077<0437:TNYRP>2.0.CO;2)

34. Kessler WS (2001) EOF Representations of the Madden-Julian Oscillation and Its Connection with ENSO. *J Clim* 14:3055–3061. [https://doi.org/10.1175/1520-0442\(2001\)014<3055:EROTMJ>2.0.CO;2](https://doi.org/10.1175/1520-0442(2001)014<3055:EROTMJ>2.0.CO;2)
35. Lee RW et al (2019) ENSO Modulation of MJO Teleconnections to the North Atlantic and Europe. *Geophys Res Lett* 46:13535–13545. <https://doi.org/10.1029/2019GL084683>
36. Liebmann B, Allured D (2005) Daily Precipitation Grids for South America. *Bull Am Meteor Soc* 86:1567–1570. <https://doi.org/10.1175/BAMS-86-11-1567>
37. Liebmann B, Smith CA (1996) Description of a Complete (Interpolated) Outgoing Longwave Radiation Dataset, *Bull Am Meteor Soc* 77:1275-1277. <https://www.jstor.org/stable/26233278>
38. Lorrey A et al (2012) Reconstructing the South Pacific Convergence Zone Position during the Presatellite Era: A La Niña Case Study. *Mon Weather Rev* 140:3653–3668. <https://doi.org/10.1175/MWR-D-11-00228.1>
39. Matsuno T (1966) Quasi-Geostrophic Motions in the Equatorial Area. *J Meteorol Soc Jpn* 44:25–43. https://doi.org/10.2151/jmsj1965.44.1_25
40. Moon JY, Wang B, Ha K (2011) ENSO regulation of MJO teleconnection. *Clim Dyn* 37:1133–1149. <https://doi.org/10.1007/s00382-010-0902-3>
41. Nogués-Paegle J, Mo KC (1997) Alternating Wet and Dry Conditions over South America during Summer. *Mon Weather Rev* 125:279–291. [https://doi.org/10.1175/1520-0493\(1997\)125<0279:AWADCO>2.0.CO;2](https://doi.org/10.1175/1520-0493(1997)125<0279:AWADCO>2.0.CO;2)
42. Paegle JN, Byerle LA, Mo KC (2000) Intraseasonal Modulation of South American Summer Precipitation. *Mon Weather Rev* 128:837–850. [https://doi.org/10.1175/1520-0493\(2000\)128<0837:IMOSAS>2.0.CO;2](https://doi.org/10.1175/1520-0493(2000)128<0837:IMOSAS>2.0.CO;2)
43. Pohl B, Matthews AJ (2007) Observed Changes in the Lifetime and Amplitude of the Madden-Julian Oscillation Associated with Interannual ENSO Sea Surface Temperature Anomalies. *J Clim* 20:2659–2674. <https://doi.org/10.1175/JCLI4230.1>
44. Rao VB, Hada K (1990) Characteristics of Rainfall over Brazil: Annual Variations and Connections with the Southern Oscillation. *Theor Appl Clim* 42:81–91. <https://doi.org/10.1007/BF00868215>
45. Rayner NA et al (2003) Global analyses of sea surface temperature, sea ice, and night marine air temperature since the late nineteenth century. *J Geophys Res D: Atmos* 108. <https://doi.org/10.1029/2002jd002670>
46. Richman MB (1986) Rotation of Principal Components. *J Climatol* 6:293–335
47. Ropelewski CF, Halpert MS (1987) Global and Regional Scale Precipitation Patterns Associated with the El Niño/Southern Oscillation. *Mon Weather Rev* 115:1606–1626. [https://doi.org/10.1175/1520-0493\(1987\)115<1606:garspp>2.0.co;2](https://doi.org/10.1175/1520-0493(1987)115<1606:garspp>2.0.co;2)
48. Roundy PE et al (2010) Modulation of the Global Atmospheric Circulation by Combined Activity in the Madden-Julian Oscillation and the El Niño-Southern Oscillation during Boreal Winter. *J Clim* 23:4045–4059. <https://doi.org/10.1175/2010JCLI3446.1>

49. Slingo JM et al (1999) On the predictability of the interannual behaviour of the Madden-Julian Oscillation and its relationship with El Niño. *Q J R Meteorol Soc* 125:583–609
50. Souza EB, Ambrizzi T (2006) Modulation of the intraseasonal rainfall over tropical Brazil by the Madden-Julian oscillation. *Int J Climatol* 26:1759–1776
51. Tam CY, Lau NC (2005) Modulation of the Madden-Julian Oscillation by ENSO: Inferences from Observations and GCM Simulations. *J Meteorol Soc Jpn* 83:727–743. <https://doi.org/10.2151/jmsj.83.727>
52. Tedeschi RG, Grimm AM, Cavalcanti IFA (2015) Influence of Central and East ENSO on extreme events of precipitation in South America during austral spring and summer. *Int J Climatol* 35:2045–2064. <https://doi.org/10.1002/joc.4106>
53. Tedeschi RG, Grimm AM, Cavalcanti IFA (2016) Influence of Central and East ENSO on precipitation and its extreme events in South America during austral autumn and winter. *Int J Climatol* 36:4797–4814. <https://doi.org/10.1002/joc.4670>
54. Tseng KC, Maloney E, Barnes EA (2020) The Consistency of MJO Teleconnection Patterns on Interannual Time Scales. *J Clim* 33:3471–3486. <https://doi.org/10.1175/JCLI-D-19-0510.1>
55. Vincent EM et al (2009) Interannual variability of the South Pacific Convergence Zone and implications for tropical cyclone genesis. *Clim Dyn* 36:1881–1896. <https://doi.org/10.1007/s00382-009-0716-3>
56. Wei Y, Ren H-L (2019) Modulation of ENSO on Fast and Slow MJO Modes during Boreal Winter. *J Clim* 32:7483-7506. <https://doi.org/10.1175/JCLI-D-19-0013.1>
57. Wheeler MC, Hendon HH (2004) An All-Season Real-Time Multivariate MJO Index: Development of an Index for Monitoring and Prediction. *Mon Weather Rev* 132:1917–1932. [https://doi.org/10.1175/1520-0493\(2004\)132<1917:AARMMI>2.0.CO;2](https://doi.org/10.1175/1520-0493(2004)132<1917:AARMMI>2.0.CO;2)
58. Wilks DS (2006) *Statistical methods in the atmospheric sciences*. Academic Press, London
59. Zhang C (2005) The Madden-Julian Oscillation. *Rev Geophys* 43:RG2003
60. Zhang C, Gottschalck J (2002) SST anomalies of ENSO and the Madden-Julian Oscillation in the Equatorial Pacific. *J Clim* 15:2429–2445. [https://doi.org/10.1175/1520-0442\(2002\)015<2429:SAOEAT>2.0.CO;2](https://doi.org/10.1175/1520-0442(2002)015<2429:SAOEAT>2.0.CO;2)
61. Zhang C, Ling J (2017) Barrier Effect of the Indo-Pacific Maritime Continent on the MJO: Perspectives from Tracking MJO Precipitation. *J Clim* 30:3439–3459. <https://doi.org/10.1175/JCLI-D-16-0614.1>

Tables

Table 1: Dates of El Niño (EN), La Niña (LN) and neutral (NT) years, obtained from the factor score classification in Figure 1

El Niño (EN)	1982/83, 1986/87, 1991/92, 1994/95, 1997/98, 2002/03, 2006/07, 2009/10
La Niña (LN)	1984/85, 1985/86, 1988/89, 1995/96, 1998/99, 1999/00, 2000/01, 2005/06, 2007/08, 2008/09
Neutral (NT)	1978/79, 1979/80, 1980/81, 1981/82, 1983/84, 1987/88, 1989/90, 1990/91, 1992/93, 1993/94, 1996/97, 2001/02, 2003/04, 2004/05

Figures

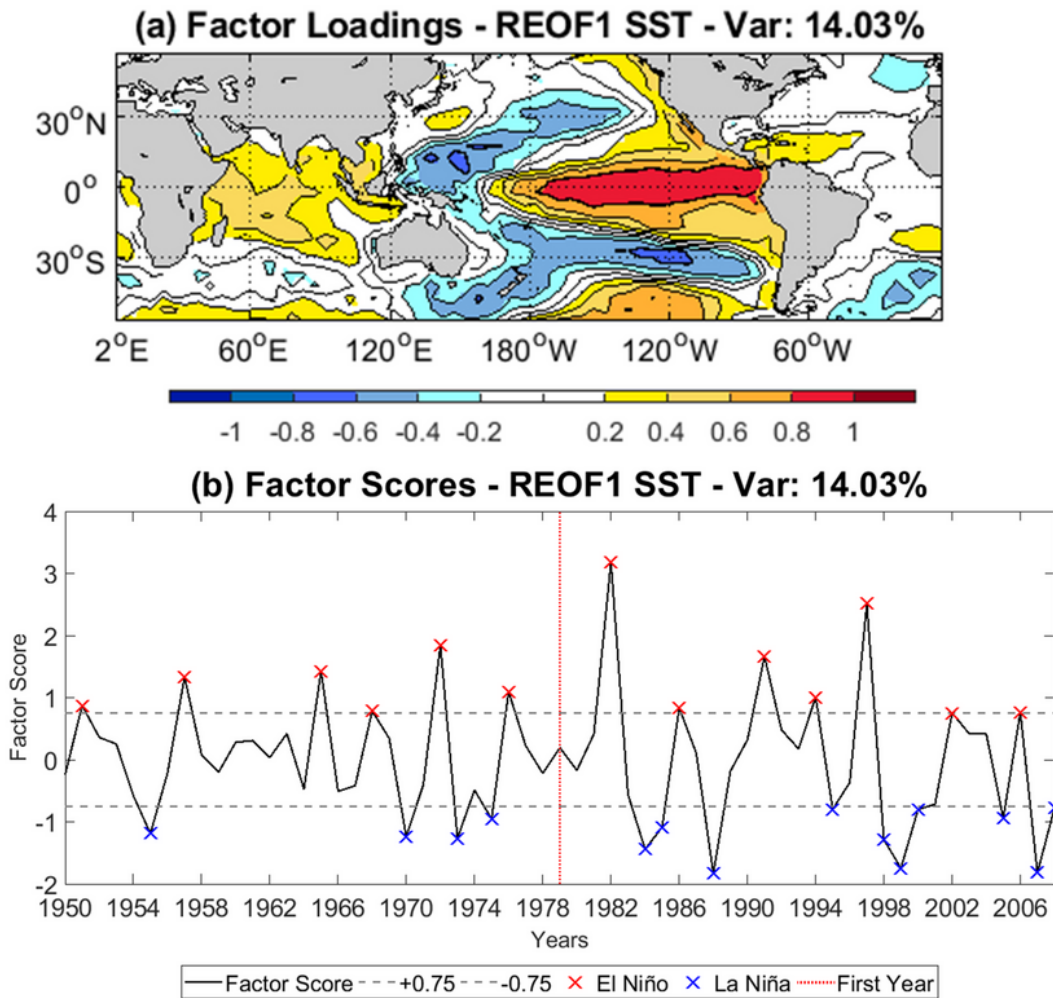


Figure 1

(a) Factor Loadings and (b) Factor Scores of the first rotated variability mode obtained from PCA analysis of SST anomalies in DJF, representing ENSO. Red (blue) crosses indicate the years classified as EN (LN). The vertical dotted red line indicates the initial date of the present analysis

(1979)

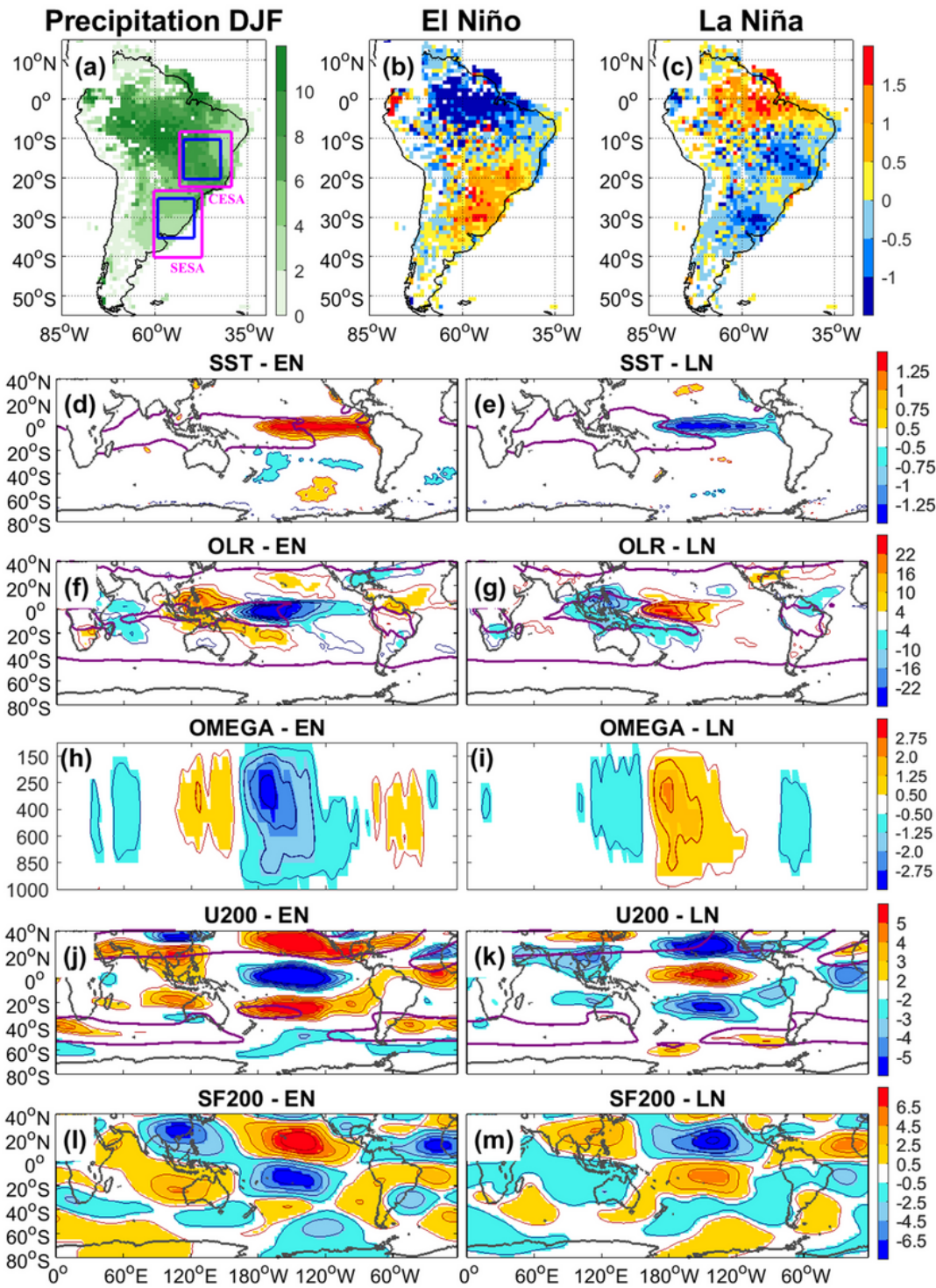


Figure 2

Top panels: (a) DJF climatological daily precipitation in South America and its anomalies for (b) EN and (c) LN (mm day^{-1}) (Table 1). Panel (a) shows, within pink lines, regions cited in the text, and within blue lines the dipole action centers of the first intraseasonal summer precipitation variability mode. The other

panels show changes in the DJF basic state produced by (left) El Niño and (right) La Niña: (d,e) SST ($^{\circ}\text{C}$); (f,g) OLR (Wm^{-2}); (h,i) Longitude-height section of omega averaged over $0\text{-}15^{\circ}\text{S}$ ($10^{-2} \text{ Pa s}^{-1}$); (j,k) 200 hPa zonal wind (ms^{-1}); (l,m) 200 hPa eddy streamfunction ($10^6 \text{ m}^2 \text{ s}^{-1}$). Reference values for SST, OLR and U200 for EN and LN are indicated by purple lines (see text)

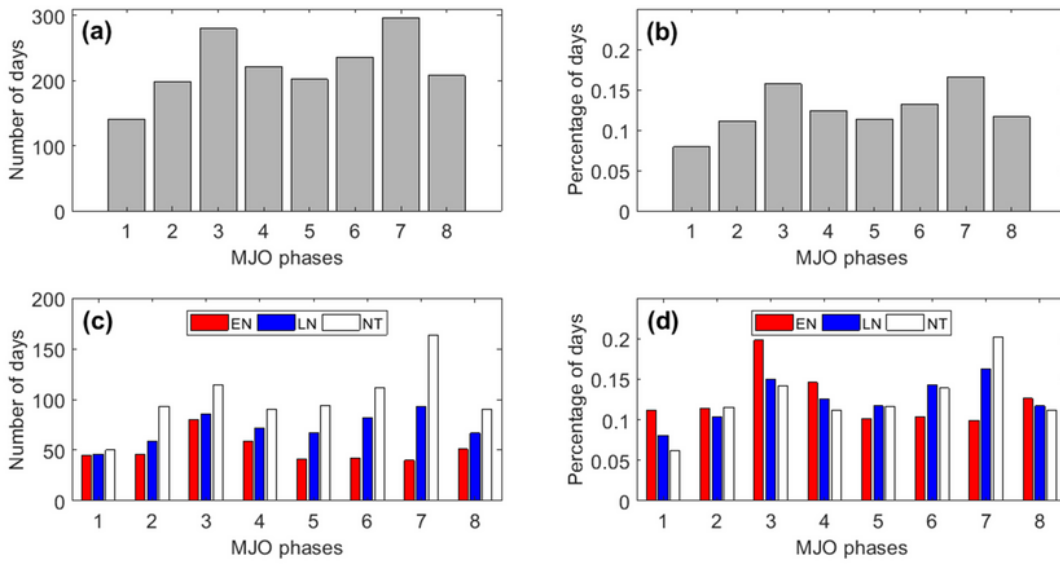


Figure 3

(a) Number of MJO active days in each MJO phase, and (b) the respective percentage of MJO active days in each MJO phase. (c) Number of active MJO days in each ENSO state, and (d) the respective percentage, considering the total of days in each ENSO phase (red for EN, blue for LN, and white for NT)

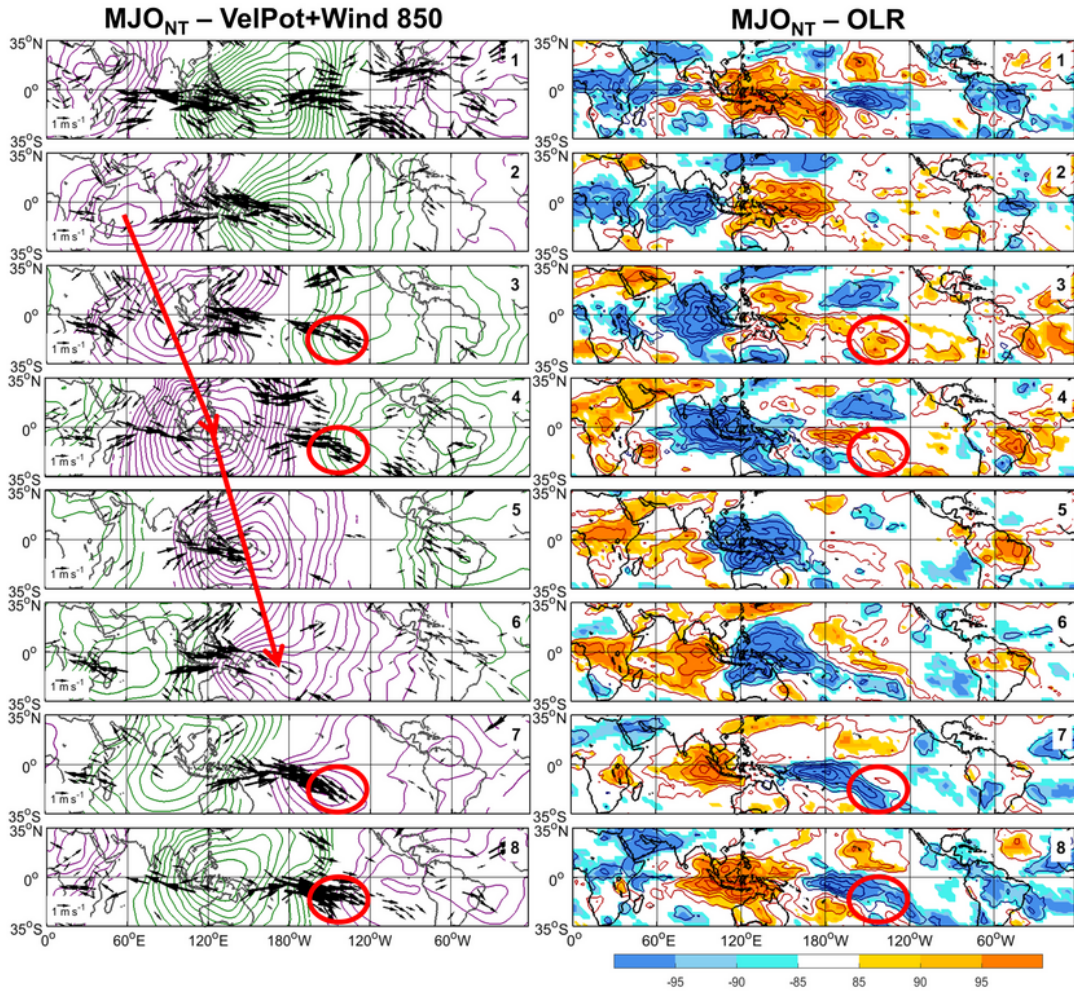


Figure 4

(Left) Composite anomalies of 850 hPa winds and velocity potential filtered in the 20–90 day band for each MJO phase during the austral summer in NT years. Contour interval is $2 \times 10^5 \text{ m}^2 \text{ s}^{-1}$. Velocity potential negative anomalies are in green and positive anomalies are in purple, with their maximum absolute values indicating centers of anomalous divergence and convergence, respectively. Only wind anomalies (ms^{-1}) with confidence levels better than 85% are shown. (Right) Composite anomalies of OLR in each MJO phase for austral summer in NT years. Contour interval is 5.0 W/m^2 . The color bar indicates confidence levels for OLR anomalies, with signs indicating positive or negative anomalies

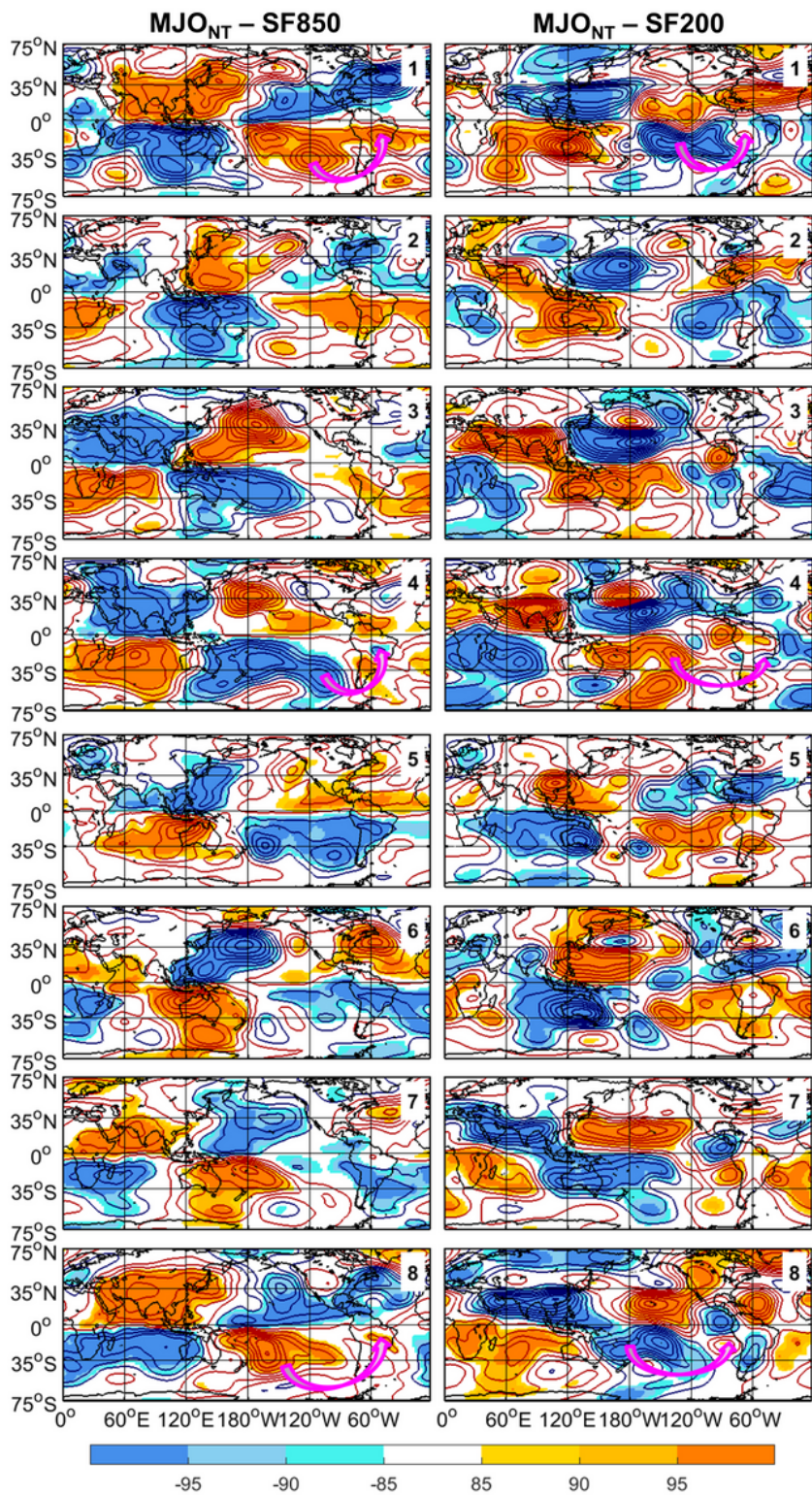


Figure 5

Composite anomalies of (left) 850 hPa and (right) 200 hPa eddy streamfunction filtered in the 20-90 day band, for each MJO phase during the austral summer (DJF) in NT years. Contour interval is 6.0×10^5 m^2s^{-1} at 850 hPa and 12×10^5 m^2s^{-1} at 200 hPa; zero line is omitted. The color bar indicates confidence levels, with signs indicating positive or negative anomalies.

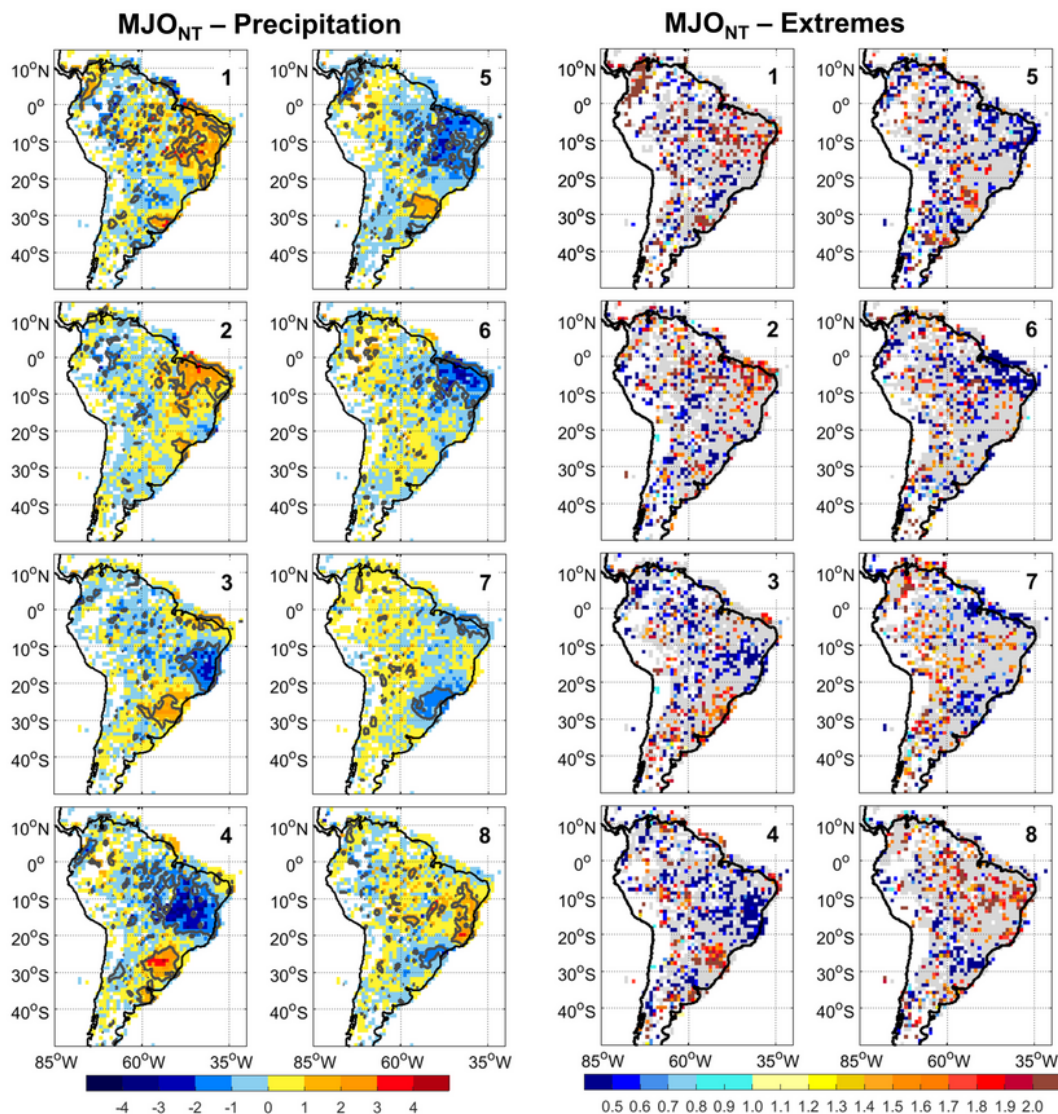


Figure 6

(Left) Composite anomalies of daily precipitation rate (color bar, mm day⁻¹) filtered in the 20–90 day band, for each MJO phase during the austral summer (DJF) in NT years. Gray lines delimit anomalies with confidence levels better than 85%. (Right) Ratio between the probability of extreme precipitation events in each of the MJO phases in NT years and the mean probability for DJF. Only ratios corresponding to statistically significant difference between the probability of occurrence for each MJO

phase and the mean probability with confidence levels better than 85% are shown in color. Grey indicates regions with lower confidence level, and white indicates regions void of observed gauge daily data

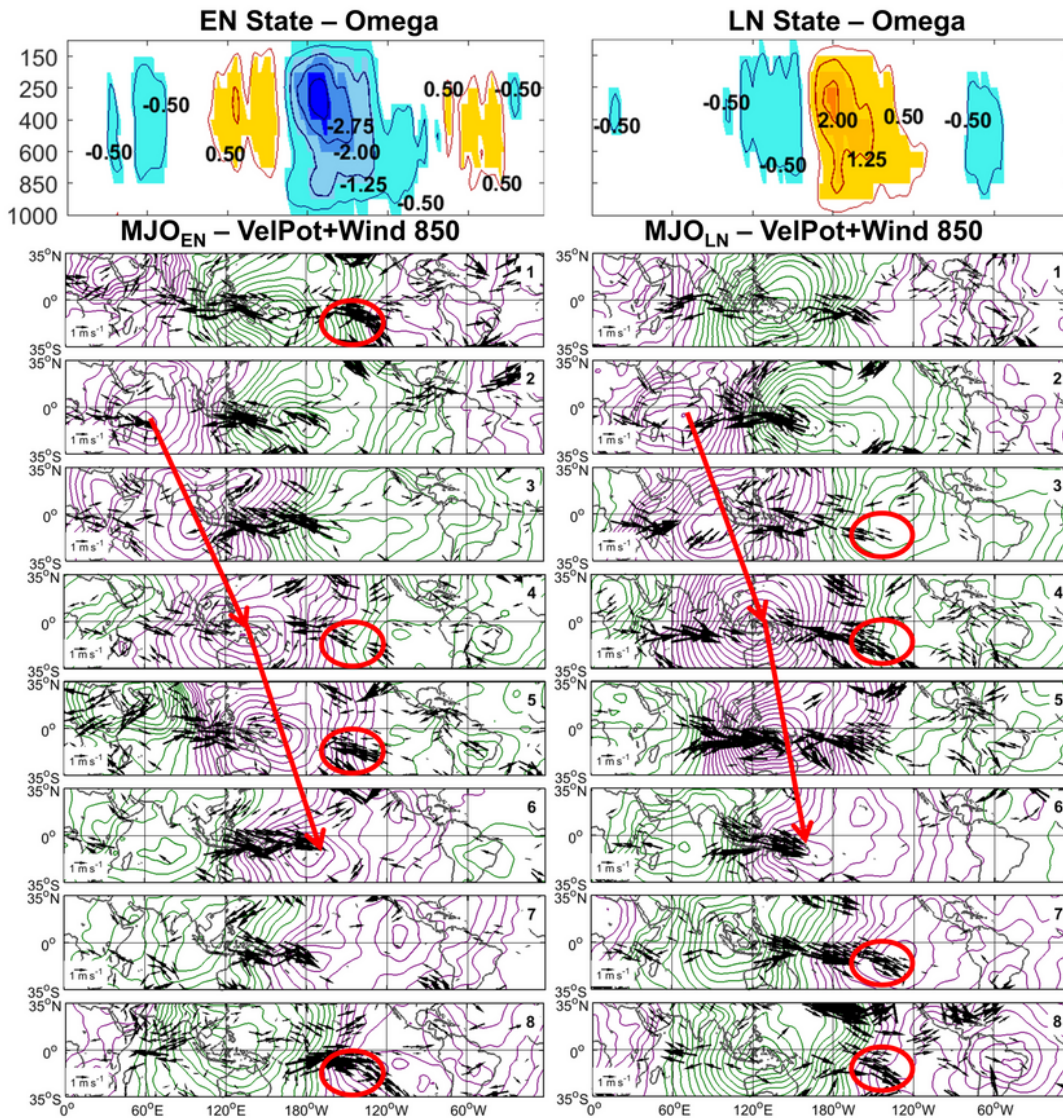


Figure 7

(Upper panels) Composite anomalies of omega ($10^{-2} \text{ Pa s}^{-1}$) for (left panel) EN state and (right panel) LN state. (Other panels) Composite anomalies of 850 hPa winds and velocity potential filtered in the 20–90

day band for each MJO phase during the austral summer in (left) EN state and (right) La Niña state. Contour interval is $2 \times 10^5 \text{ m}^2 \text{ s}^{-1}$. Velocity potential negative anomalies are in green and positive anomalies are in purple, with their maximum absolute values indicating centers of anomalous divergence and convergence, respectively. Only wind anomalies (ms^{-1}) with confidence levels better than 85% are shown

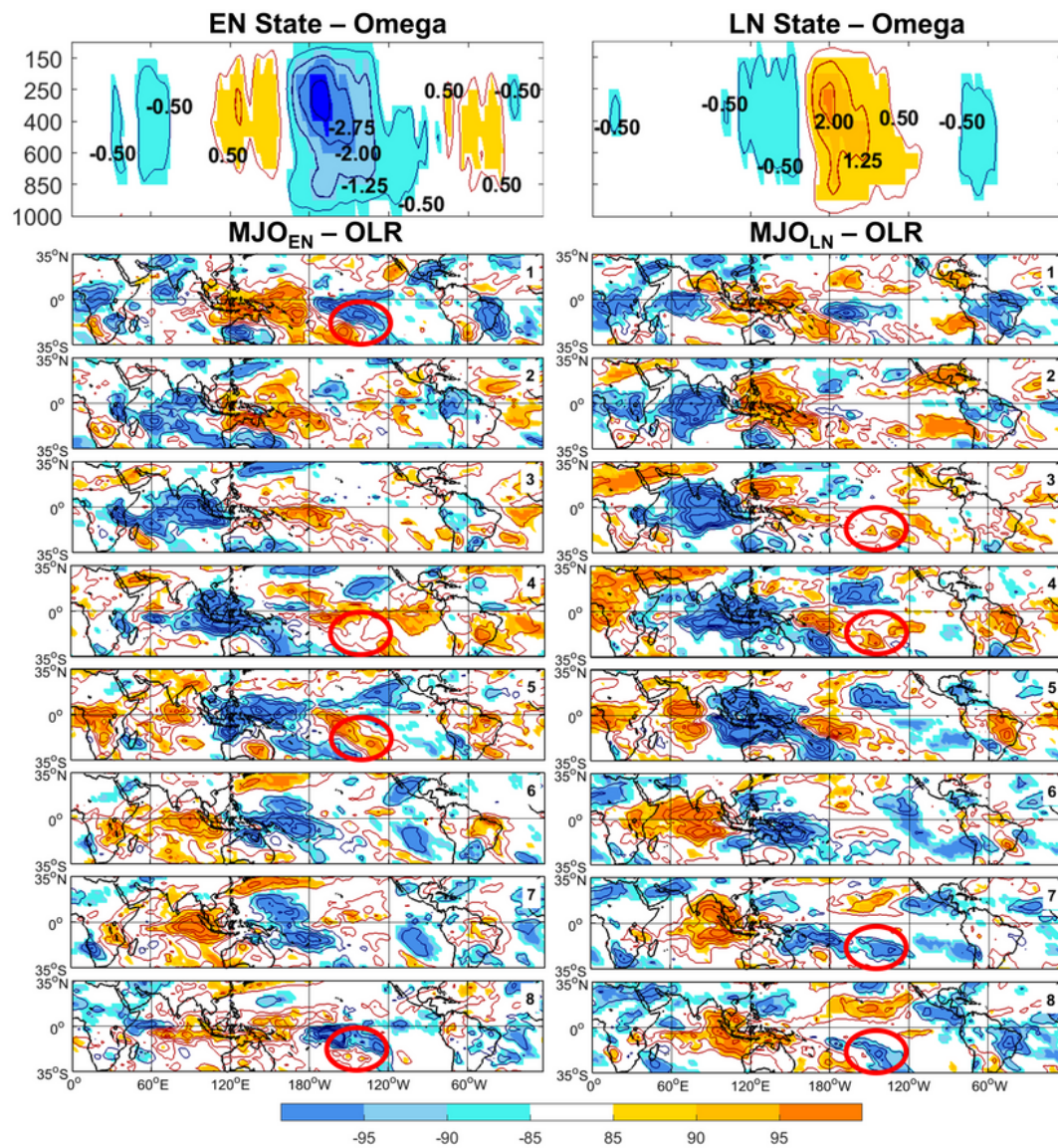


Figure 8

(Upper panels) Composite anomalies of omega ($10^{-2} \text{ Pa s}^{-1}$) for (left panel) EN state and (right panel) LN state. (Other panels) Composite anomalies of OLR filtered in the 20–90 day band for each MJO phase during the austral summer in (left) EN state and (right) La Niña state. Contour interval is 5.0 W/m^2 . The color bar indicates confidence levels, with signs indicating positive or negative anomalies

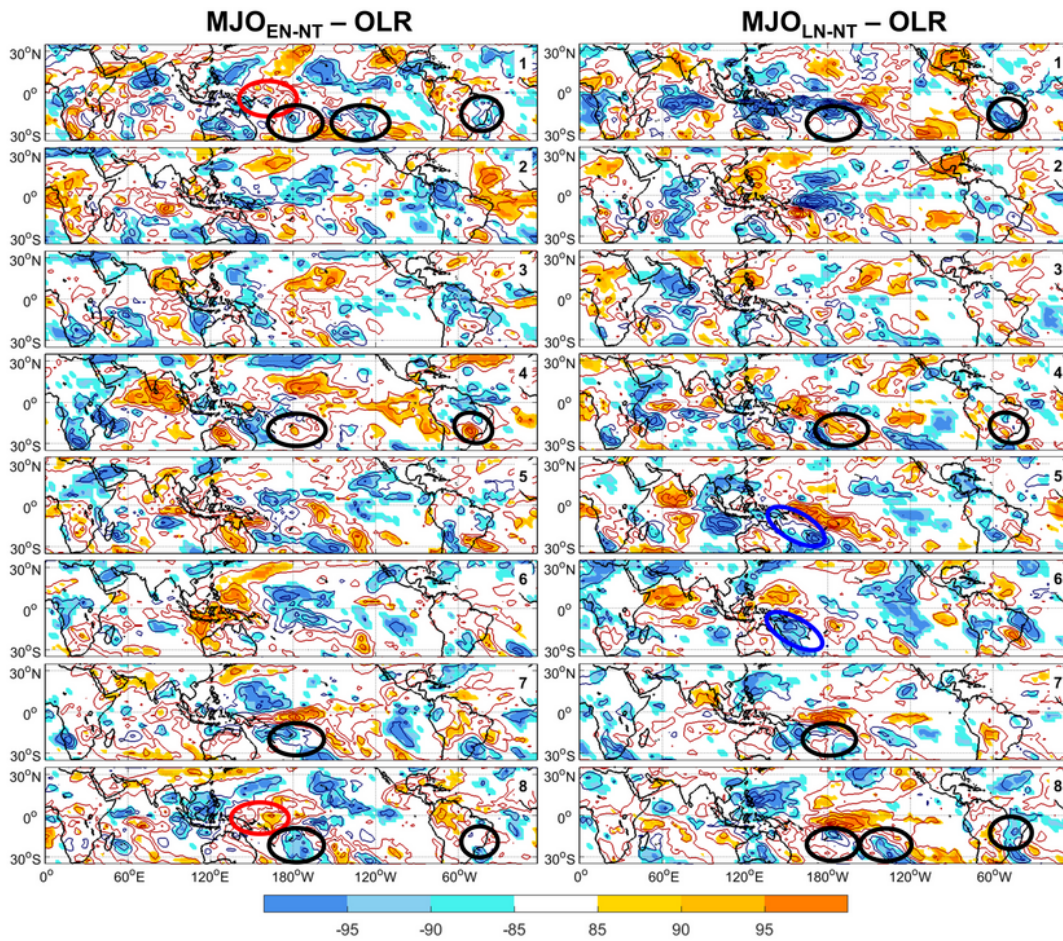


Figure 9

(Left panels) Difference between composite anomalies of OLR in the 20–90 day band for each MJO phase during the austral summer for EN years and NT years. Contour interval is 5.0 W/m^2 . The color bar indicates confidence levels, with signs indicating positive or negative differences. The red ellipses show the enhancement of subsidence over western Pacific in phases 8 and 1, when the strongest subsidence associated with the MJO coincides with the strongest subsidence associated with EN. (Right panels) Same difference, but for LN years and NT years. The blue ellipses show the enhancement of convection over western Pacific in phases 5 and 6, when the strongest convection associated with the MJO coincides with the strongest convection associated with LN. The black ellipses indicate that the subtropical regions in central-eastern South Pacific that are efficient in triggering a Rossby wave train towards South America (according to the Influence Functions of Grimm 2019), present similar convection anomalies during MJO phases 7 and 8 in EN and LN, and, therefore, similar effects on this teleconnection in both ENSO states, although it is earlier established in LN than in EN. Therefore, both states enhance the precipitation anomalies in CESA (and SACZ), but its strongest effect happens one phase earlier during LN (phase 8) than during EN (phase 1).

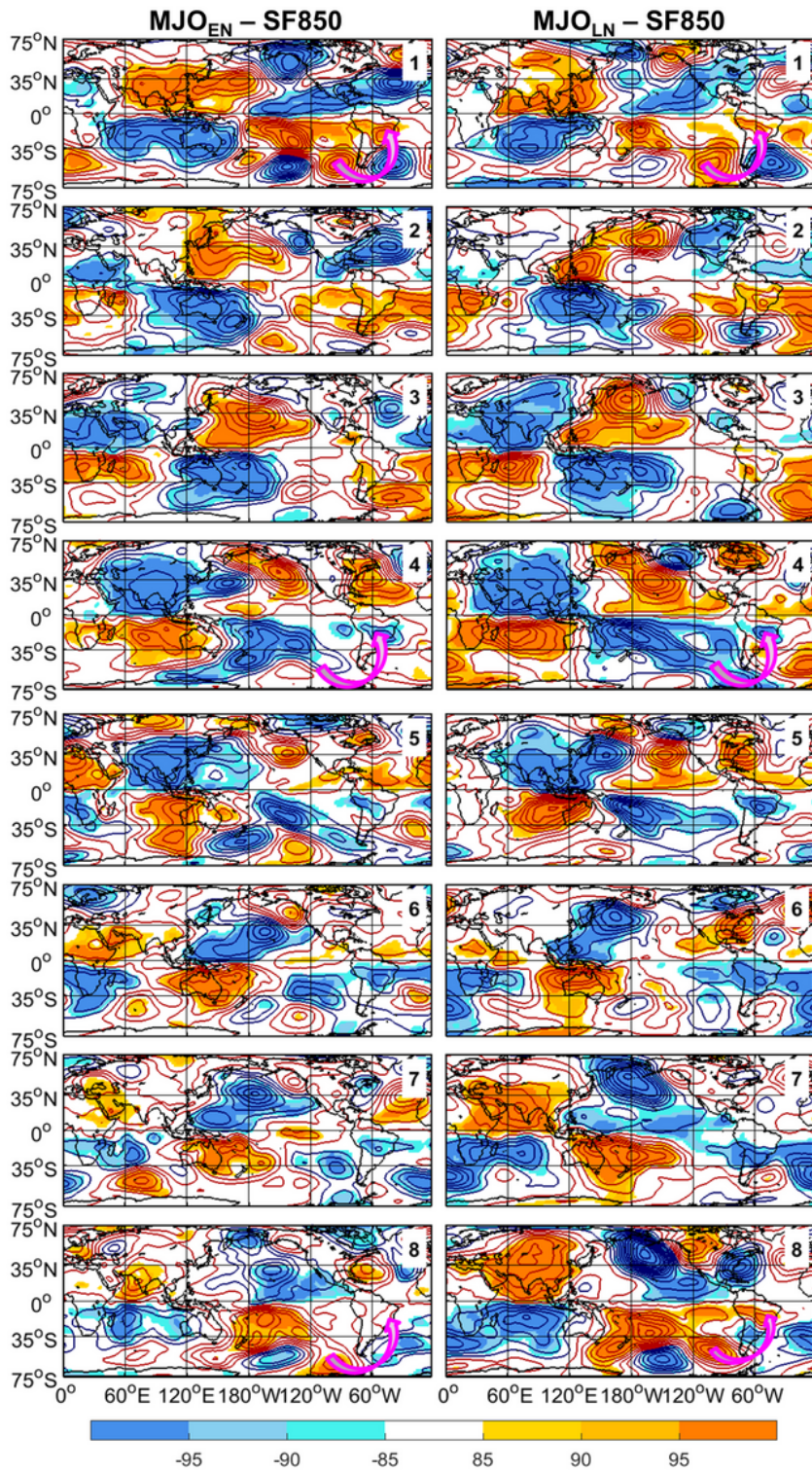


Figure 10

Composite anomalies of 850 hPa streamfunction filtered in the 20-90 day band, for each MJO phase during the austral summer (DJF) in (left) El Niño state and (right) La Niña state. Contour interval is $6.0 \times 10^5 \text{ m}^2 \text{ s}^{-1}$; zero line is omitted. The color bar indicates confidence levels, with signs indicating positive or negative anomalies

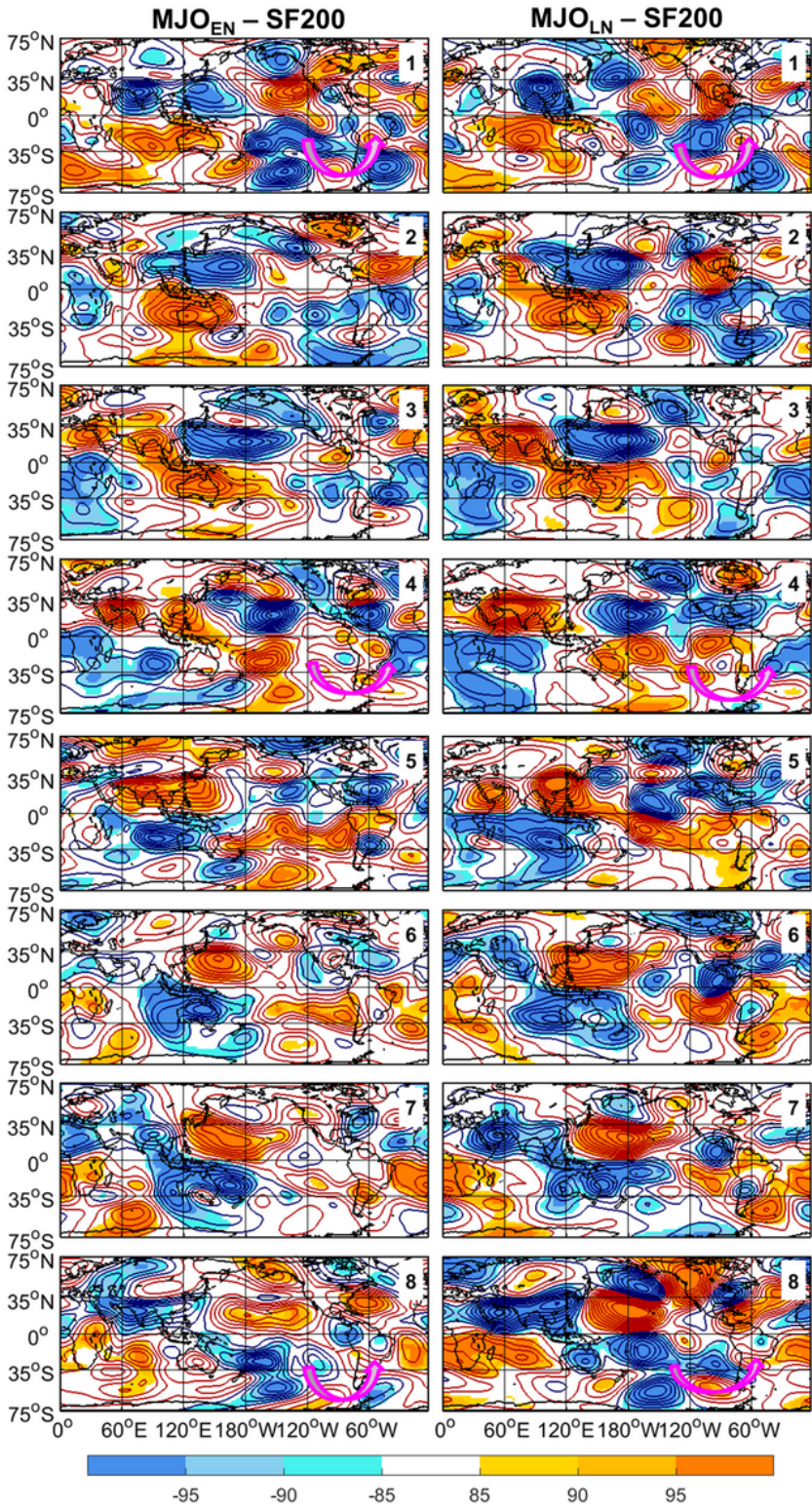


Figure 11

Composite anomalies of 200 hPa streamfunction filtered in the 20-90 day band, for each MJO phase during the austral summer (DJF) in (left) EN state and (right) La Niña state. Contour interval is 12×10^5

m^2s^{-1} ; zero line is omitted. The color bar indicates confidence levels, with signs indicating positive or negative anomalies

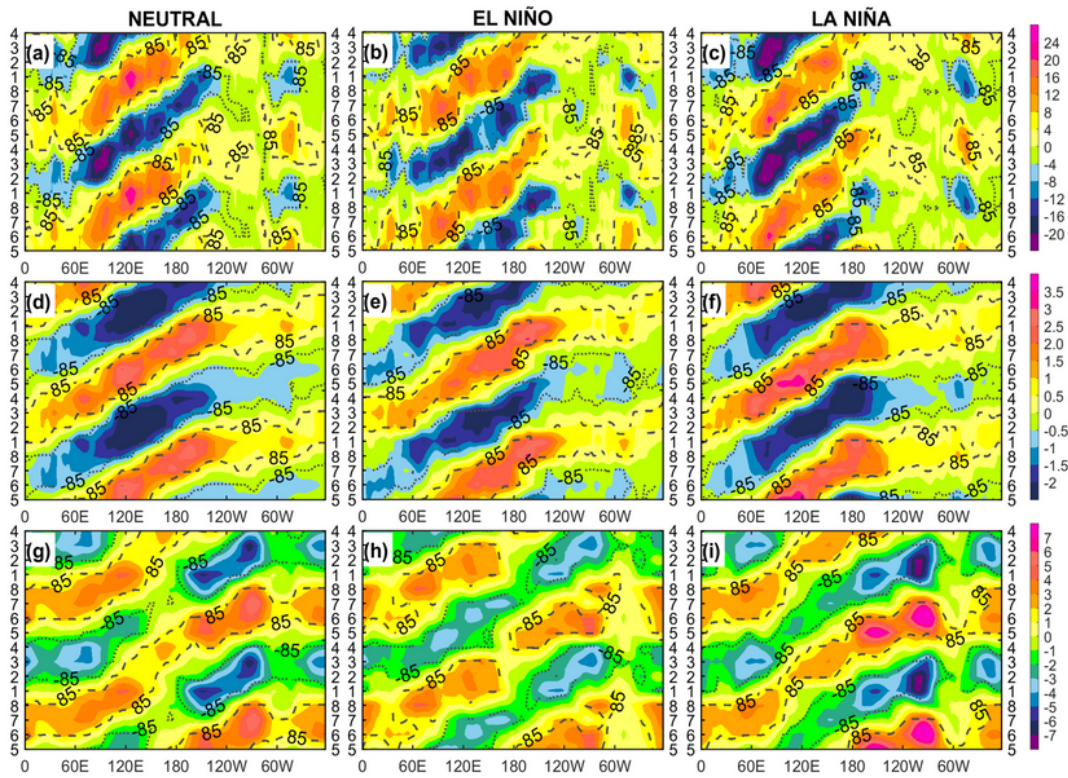


Figure 12

(a, b, c) MJO phase-longitude Hovmoller diagrams of OLR anomalies (Wm^{-2}); (d, e, f) zonal wind anomalies at 850 hPa (ms^{-1}), and (g, h, i) 200 hPa (ms^{-1}), averaged over 0° - 15°S , during the austral

summer. Left panels for NT, middle panels for EN and right panels for LN. The dotted and dashed lines delimit the significant values with confidence levels better than 85%

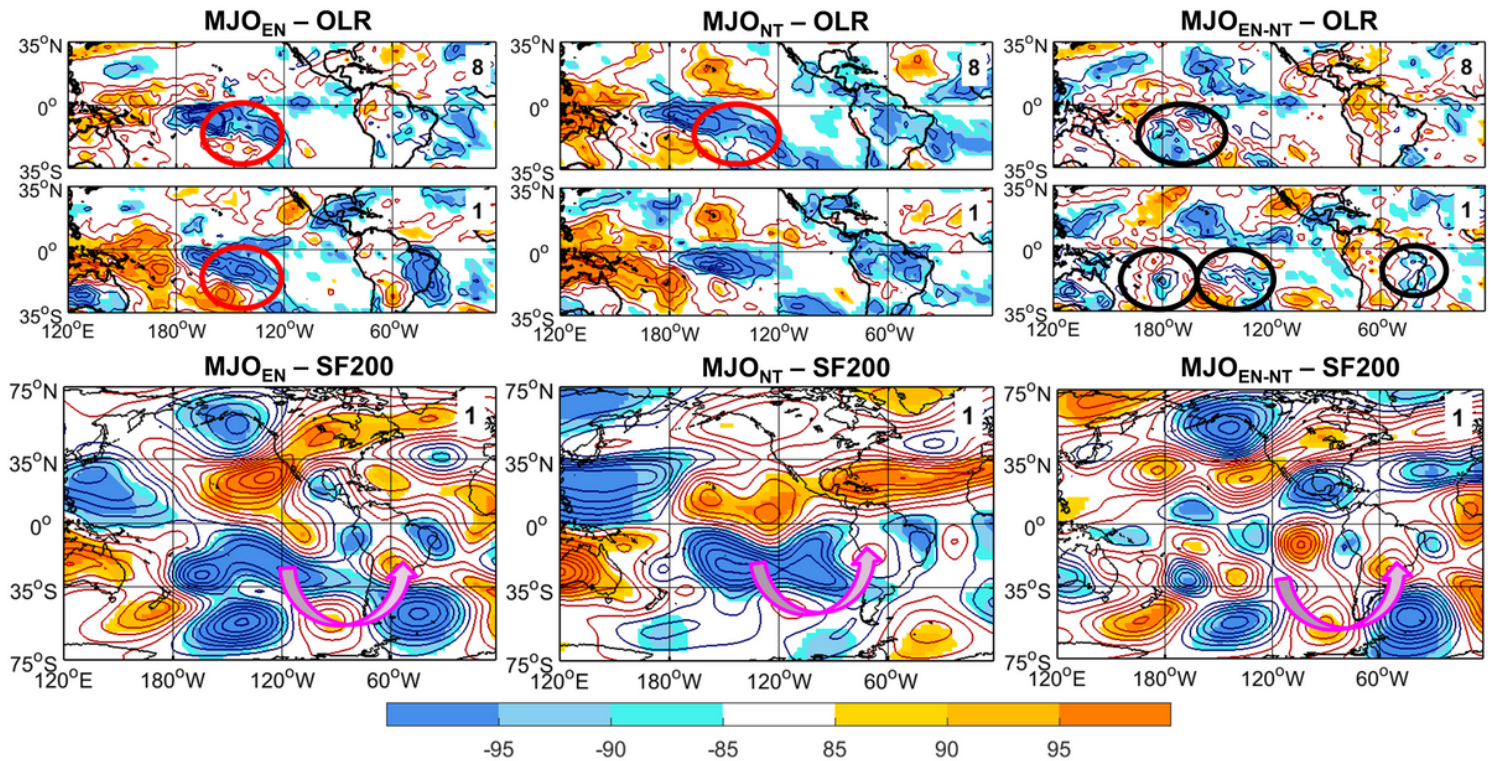


Figure 13

(Left panels) Zoom on the Western Hemisphere composite anomalies filtered in the 20–90 day band of OLR for MJO phases 8 and 1 and of 200 hPa streamfunction for MJO phase 1 during the austral summer in EN state (taken from Figs. 8 and 11). (Central panels) the same for NT state (taken from Figs. 4 and 5). (Right panels) Differences EN-NT, which emphasize the enhancement during EN of the convective anomalies in the subtropical central-east South Pacific, the strengthening of the extratropical teleconnection towards SA and the increase of convection over CESA (and SACZ). Contour interval for OLR is 5.0 W/m^2 , and for streamfunction is $12 \times 10^5 \text{ m}^2 \text{ s}^{-1}$. Zero line is omitted

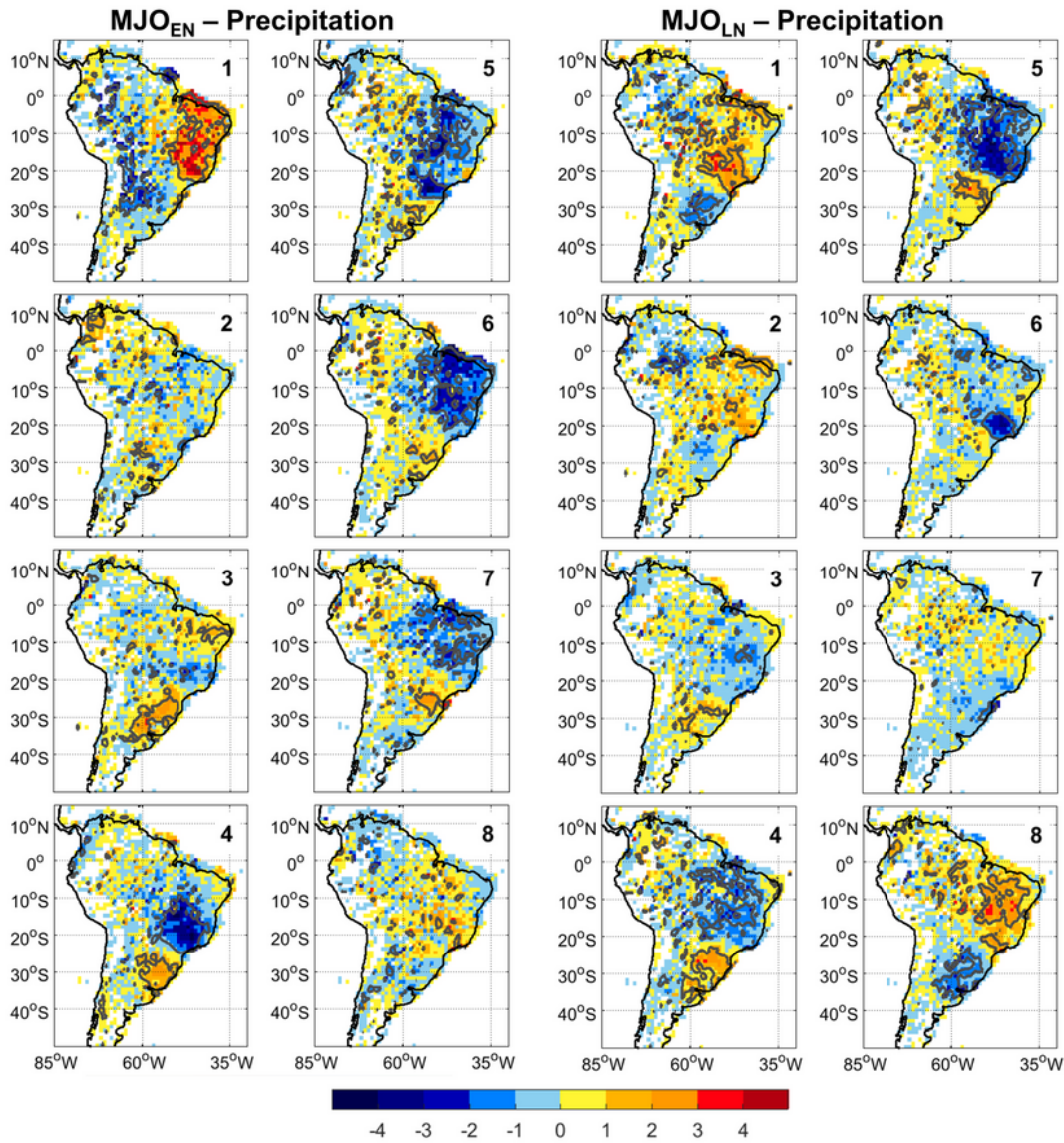


Figure 14

Composite anomalies of austral summer daily precipitation rate (color bar, mm day⁻¹) filtered in the 20–90 day band, for each MJO phase during the austral summer (DJF) in (left) El Niño state and (right) La Niña state. Gray lines delimit anomalies with confidence levels better than 85%

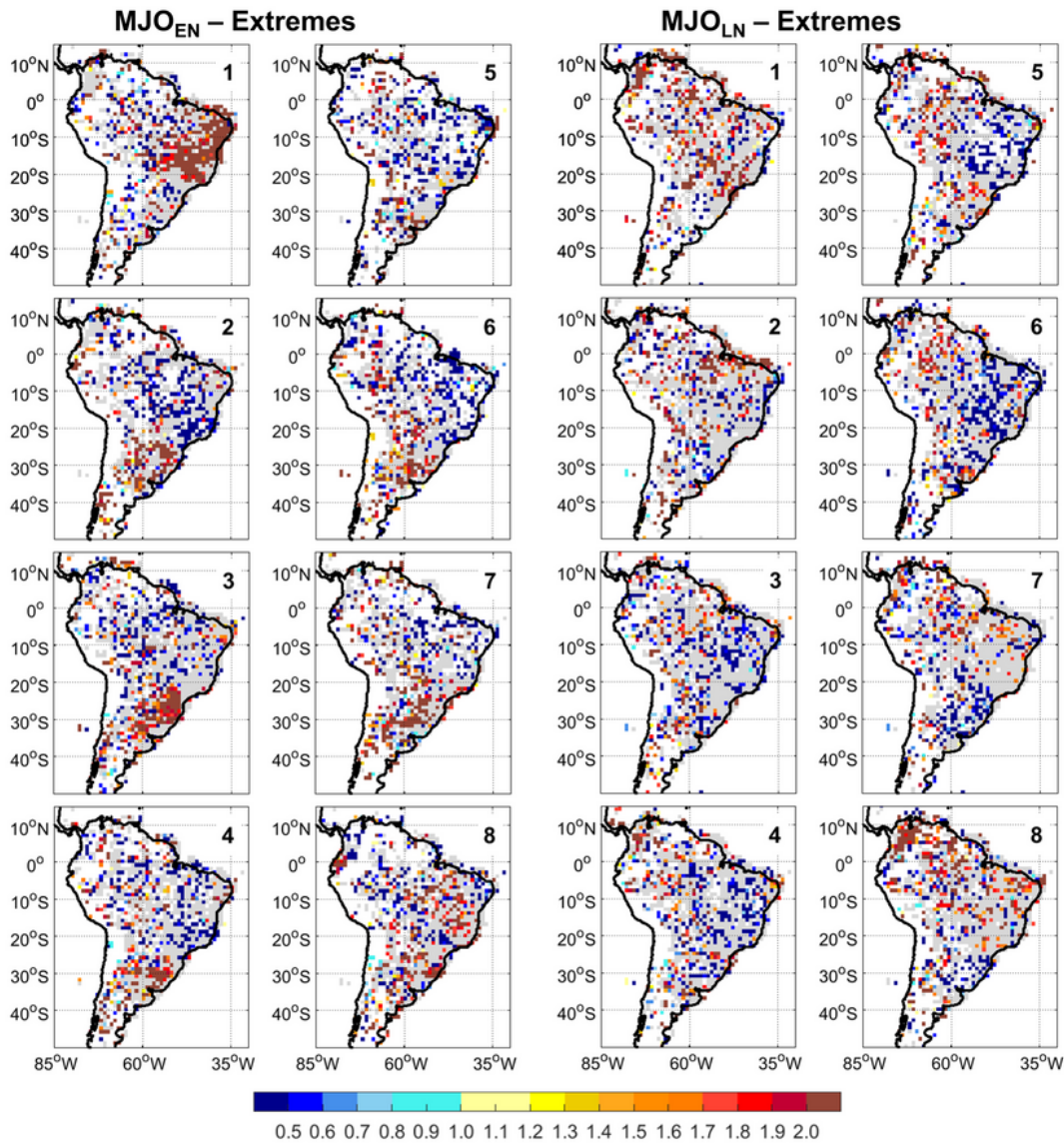


Figure 15

Ratio between the probability of extreme precipitation events in each of the MJO phases and the mean probability, for each MJO phase during the austral summer (DJF) in (left) El Niño state and (right) La Niña state. Only ratios corresponding to statistically significant difference between the probability of occurrence for each MJO phase and the mean probability with confidence levels better than 85% are

shown in color. Grey indicates regions with lower confidence levels, and white indicates regions void of observed gauge daily data

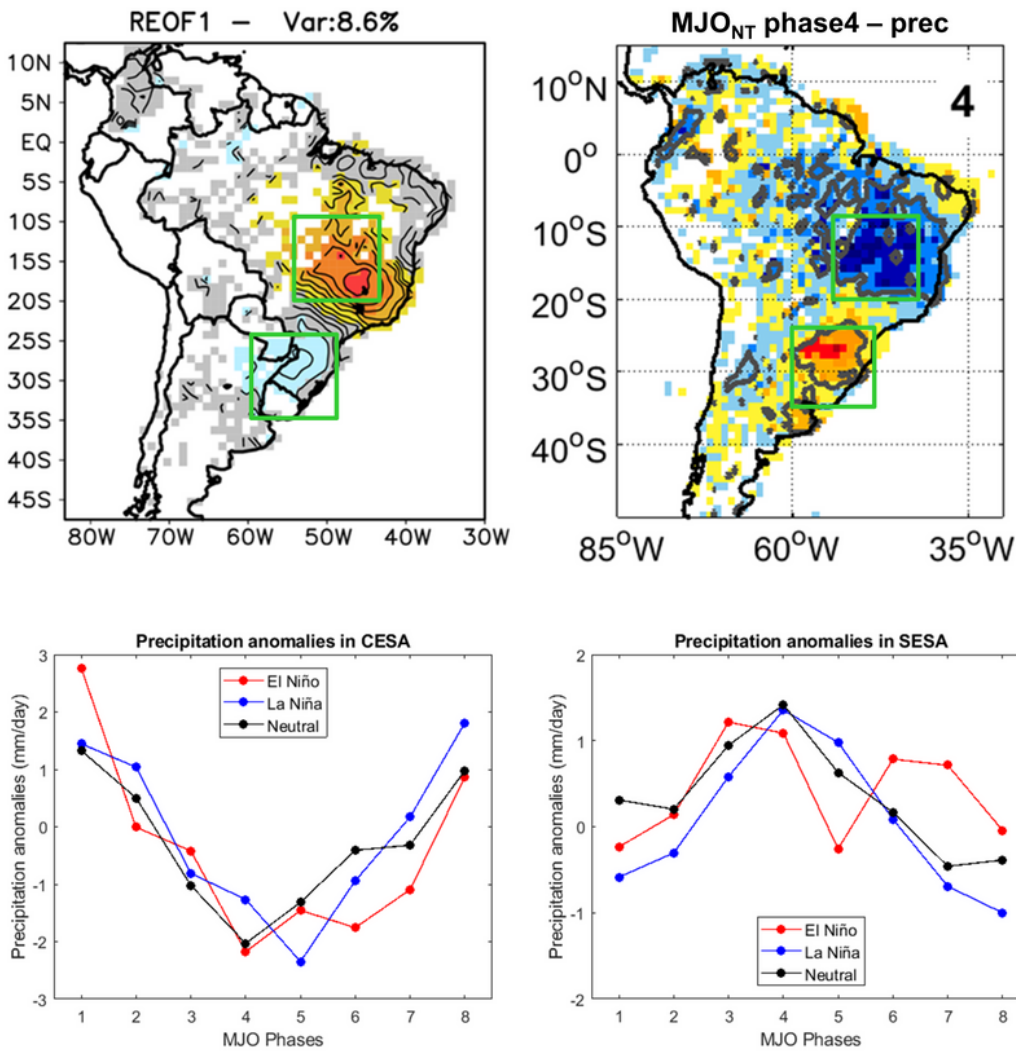


Figure 16

Upper panels: (Left) Factor loadings of the first intraseasonal variability mode of daily precipitation in the 20-90 day band for South America (from Grimm 2019), and (Right) composite anomalies of daily precipitation rate filtered in the 20–90 day band, for MJO phase 4 during the austral summer (DJF) in NT years, taken from Fig. 6. In both maps are indicated the regions representing the dipole centers of that mode, used for averaging the daily precipitation in each MJO phase and ENSO state shown in the bottom panels. Bottom panels: (Left) average daily precipitation anomalies observed during DJF and stratified by ENSO state and MJO phase over the region representing the northern center of the first variability mode (in CESA), and (Right) over the region representing the southern center of the first variability mode (in SESA)